Department for Physics and Astronomy
University of Heidelberg

Bachelor Thesis in Physics
submitted by

Jonas Bechtel

born in Heidelberg (Germany)

April 2022

Cooling force measurements with the phase shift method at the cryogenic storage ring CSR

This Bachelor Thesis has been carried out by Jonas Bechtel at the
Max Planck Institute for Nuclear Physics in Heidelberg
under the supervision of
Dr. Holger Kreckel and Dr. Oldřich Novotný

Abstract

The electron cooler at the cryogenic storage ring CSR located at the Max Planck Institut für Kernphysik is used for ion beam phase space cooling, with the benefit of reaching a low ion energy spread relevant, e.g., for collision studies at conditions found in interstellar medium. The electron cooling quality is implied by the cooling force, which depends on various experimental parameters. In this thesis a phase-shift method for the electron cooling force measurement and electron cooling optimization is presented. It was successfully implemented and tested by recording data for four ion beam types: Xe^{3+}, ArH^{+}, HeH^{+} and Ne^{2+}. The data was evaluated and the resulting cooling force curves were analysed for various systematic effects. Also a theoretical model to calculate the cooling force is given and the experimental results are compared with numerically calculated cooling force curves. The model was found to describe the experimental results well. Based on this work, the cooling force measurement is expected to become a routine optimization method in the CSR experiments involving electron beams.

Zusammenfassung

Der Elektronenkühler am kryogenen Speicherring CSR am Max-Planck-Institut für Kernphysik wird für Ionenstrahl-Phasenraumkühlung verwendet, mit dem Vorteil, dass eine geringe Ionenenergieverteilung erreicht wird, die z.B. für Kollisionsstudien unter Bedingungen wie in interstellaren Medium relevant ist. Die Qualität der Elektronenkühlung wird durch die Kühlkraft impliziert, die von verschiedenen experimentellen Parametern abhängt. In dieser Arbeit wird ein Phasenverschiebungsverfahren zur Messung der Elektronenkühlkraft und Optimierung der Elektronenkühlung vorgestellt. Es wurde erfolgreich implementiert und getestet, indem Daten für vier Ionenstrahltypen aufgezeichnet wurden: Xe^{3+}, ArH^{+}, HeH^{+} und Ne^{2+}. Die Daten wurden ausgewertet und die resultierenden Kühlkraftkurven auf verschiedene systematische Effekte analysiert. Außerdem wird ein theoretisches Modell zur Berechnung der Kühlkraft angegeben und die experimentellen Ergebnisse mit numerisch berechneten Kühlkraftkurven verglichen. Es wurde festgestellt, dass das Modell die experimentellen Ergebnisse gut beschreibt. Basierend auf dieser Arbeit soll die Kühlkraftmessung zu einer routinemäßigen Optimierungsmethode in den CSR-Experimenten mit Elektronenstrahlen werden.

Contents

List of Figures

List of Tables

1. Introduction

In the Cryogenic Storage Ring (von Hahn *et al.* 2016) conditions similar to the ones in an interstellar medium are mimicked in order to study molecular clouds consisting of large amounts of interstellar medium, which are the beginning of star formation in the universe. In these low density molecular clouds ions with very low internal and kinematic temperatures of 30 - 100 K (Snow & McCall 2006) can be found. In CSR the low internal temperatures are achieved by cooling the entire ring down to ≈ 6 K, enabling ions to undergo radiative deexcitation until they are in a much lower rotational and vibrational state reducing their internal temperature. This mimicks the lack of infrared radiation in molecular clouds. In order to reduce kinematic or collision energies between ions, an electron cooler is used. It creates a nearly monoenergetic electron beam, that is overlapped with the ion beam and transports the relative energy of the ions out of system. This decreases the energy spread and size of the ion beam, a necessity for other precise measurements using the ion beam. This effect is characterised by the cooling force, which defines the necessary time to achieve an equilibrium state as well as the achievable size of the ion beam. A direct measuring method of the cooling force is therefore useful for optimization of electron cooling.

Several reaction types can occur in the cold molecular clouds such as ion-neutral reactions and ion-electron collisions. Studying some of those reaction in CSR requires low collision energies and a good overlap with the target beam making electron cooling essential. One example is dissociative recombination, which involves a positive ion colliding with a negative electron:

$$\mathrm{AB}^+ + e^- \rightarrow \mathrm{A} + \mathrm{B} \tag{1.1}$$

Here AB^+ is a singly charged positive molecular ion, which collides with an electron e^- and breaks apart into two neutral molecule fragments A and B. Dissociative recombination is considered as the main neutralizing mechanism in interstellar matter and therefore knowledge of its reaction cross-section and reaction rate is important. Since these properties depend on the state of the ions it is necessary to simulate interstellar conditions in order to get realistic results.

The goal of the work presented in this thesis was to implement and test a measuring method called phase shift method for cooling force measurements. This was done by measuring the cooling force with several ions, comparing the effect that various settings have on it and optimizing them. Also a theoretical model was used simulate the results and compare them with experimental results.

This Bachelor thesis starts with chapter 2, where the theory of electron cooling and the measuring method that was used to obtain the data for this thesis is described. Chapter 3 will be a brief overview over the Cryogenic Storage Ring CSR and the integrated electron cooling system, where their purpose as well as the functioning principle will be explained. Afterwards in chapter 4 the analysis of the data begins. It starts with a description of the data of the four ions that were studied. Here the different ways of evaluating the data are introduced. Next follows the comparison between the cooling force curves of the same ion but with different settings. The analysis ends with the comparison of some experimental

cooling force curves with simulation results. The final chapter contains a conclusion and outlook.

2. Electron Cooling in an ion storage ring

This chapter first introduces the concept of electron cooling and its benefits followed by a theoretical model describing this effect. Then the experimental measuring method used for the thesis is explained.

2.1. Principle of Electron Cooling

The idea of electron cooling was first proposed by Budker 1967 with the intention of improving a particle beam's quality by reducing the momentum spread and size of the beam. This is achieved by overlapping the ion beam with an electron beam which now interact via Coulomb collisions.

In an ion storage ring there exists a fixed ideal ion beam trajectory called the closed orbit defined by the ion optics elements. Not all ions move on that orbit however, due to a finite phase-space distribution of the beam when injecting into the storage ring. Here phase space refers to a particles position relative to a particle traveling on the closed orbit and its relative momentum deviation to that particle. Therefore particles oscillate around the closed orbit in a direction perpendicular to the direction of flight producing so-called betatron oscillations.

One purpose of electron cooling is to dampen betatron oscillations and reduce the occupied phase-space of the ion beam. This is achieved by overlapping an electron beam with the ion beam for a certain part of the orbit, as can be seen in Figure 2.1 a). The average velocity of the electrons $\langle \vec{v}_\mathrm{e} \rangle$ is matched with the average velocity of the ions $\langle \vec{v}_i \rangle$ in the overlap region. This defines the cooling energy of the electrons, which is given by

$$E_\mathrm{cool} = \frac{m_\mathrm{e}}{m_\mathrm{ion}} E_\mathrm{ion} = \frac{m_\mathrm{e} f_\mathrm{rev}^2 C_0^2}{2}, \tag{2.1}$$

where C_0 is the circumference of the storage ring, f_rev is the ion beam revolution frequency, m_e and m_ion are the electron and ion mass, respectively, and E_ion is the kinetic energy of the ion beam. In the frame moving with the electron beam both particles move only due to their thermal energy distribution and interact with each other via Coulomb collisions. By the means of this process energy is transferred from the ions to the electrons. The latter transport the energy out of the system by being collected in a Faraday cup at the end of the electron cooler and they are continuously replaced in the interaction zone.

Ions are generally created "hotter" meaning they have a much broader energy distribution than the electrons. This is due to limitations in the ion creation process resulting in an energy distribution spread on the order of eV. The energy spread of electrons however can be controlled more easily and reduced down to the order of meV by mechanisms described in section 3.2.

All of the Coulomb collisions create an average force on the ions, that depends on the relative velocity between ions and electrons and is split into a longitudinal component parallel to the direction of travel and a transverse component perpendicular to it. The

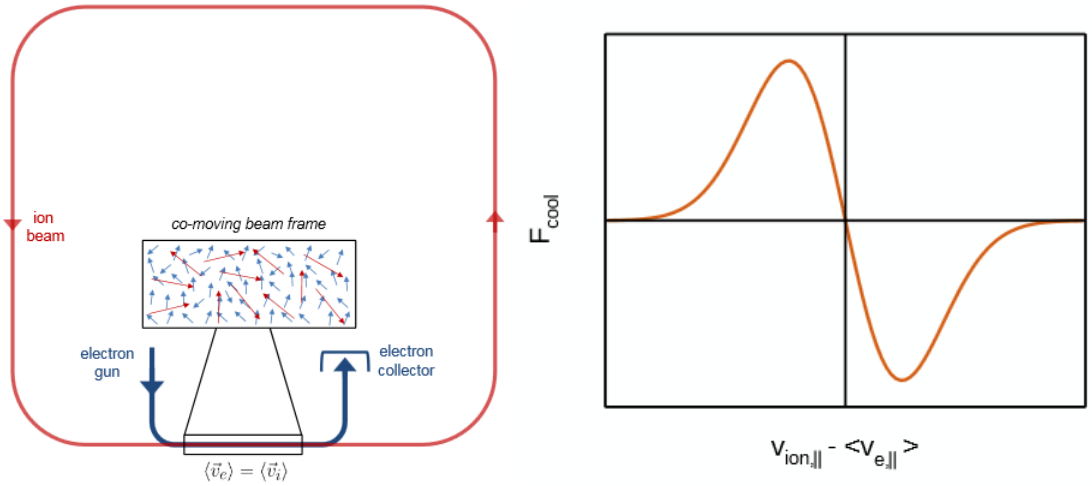

(a) (b)

Figure 2.1: Principle of electron cooling. Panel a): Ion beam (red) and electron beam (blue) are merged in a section of the ring at matched mean velocities. Particles interact via Coulomb collisions as shown in the co-moving beam frame. Panel b): Qualitative dependence of the longitudinal cooling force on the velocity difference between ions and the average electron velocity. Figures are taken from Paul 2021.

transverse part is responsible for the reduction of betatron oscillations resulting in a compression of the ion beam and a reduction of its divergence. This leads to a better overlap with the electron beam, which is necessary for electron-ion reaction experiments since they require the ion beam to be completely inside the electron beam.

The cooling force also affects the longitudinal temperature of the ions. In a coasting ion beam, consisting of a constant stream of ions, the longitudinal cooling force reduces the longitudinal energy spread of the ions. But it can also be used on a bunched beam. A bunched ion beam consist of ion bunches instead of a constant stream of ions. This can be achieved using the radio frequency (RF) bunching system of a storage ring, which will be explained in more detail in section 2.3. This causes frequency oscillations around the ideal revolution frequency, called synchrotron oscillations, that can be dampened by the longitudinal cooling force cooling force.

A qualitative dependence of the longitudinal cooling force on the velocity difference between the longitudinal velocity of a single ion $v_{\mathrm{ion}\parallel}$ and the average longitudinal electron velocity $\langle v_{\mathrm{e}\parallel} \rangle$ is presented in Figure 2.1 b). For small velocity deviations around zero the cooling force changes linearly. It reaches the extrema, close to the velocity spread of the electrons and converges back to zero with a $\sim \frac{1}{\left(v_{\mathrm{ion}\parallel} - \langle v_{\mathrm{e}\parallel} \rangle\right)^2}$ dependence for large velocity differences.

Another advantage of electron cooling is the increased ion beam lifetime that is caused by counteracting heating effects, that would otherwise lead to the loss of the ion beam. Apart from that the phase-space cooling reduces the momentum spread of the ion beam and therefore improves the achievable energy resolution.

In the case where the mean electron and ion velocities are slightly different, the cooling force drags the ion beam until their velocities are matched. This way the mean ion velocity can be defined by the electron beam energy, which might otherwise not be known very precisely. For collision experiments, where the mean electron velocity is detuned from that of the ion beam, this enables a precise knowledge of collision energies.

2.2. Binary Collision Model

To derive a mathematical expression of the cooling force a simple binary collision model will be used in this thesis. It considers both beams as a two-component plasma, where Rutherford scattering events between ions and electrons take place, in which momentum is transferred via Coulomb interactions. There is also another model called dielectric plasma description, which considers the polarisation of the electron beam by an ion. The change of the electron distribution creates an electric field, responsible for the force acting on the ions. Both models are explained by Poth 1990.

Here, the binary collision model is described based on the works of Poth 1990 and Wilhelm 2019. These considerations however will not include the longitudinal magnetic field that is usually used in electron coolers to guide the electrons through the interaction region. There is an extension to the binary collision model that includes the magnetic field (see Derbenev & Skrinsky 1978). It however makes some crucial assumptions about the possible impact parameters and is therefore not used in this thesis.

The process of Coulomb interactions is shown in Figure 2.2 a), where the ion has the relative velocity v_r compared to the electrons and b is the impact parameter of the collision. The momentum Δp, transferred to the ion is given by

$$\Delta p = \int F_{\text{Coulomb},\perp} dt = \frac{1}{4\pi\epsilon_0} \int_{-\infty}^{\infty} \frac{Ze^2}{s^2 + b^2} dt = \frac{2Ze^2}{4\pi\epsilon_0 v_r b}, \tag{2.2}$$

where ϵ_0 is the vacuum permittivity, Z is the charge state of the ion, e is the elementary charge and s is the distance shown in Figure 2.2 a). The Coulomb force F_{Coulomb} is integrated over time from negative infinity to positive infinity but only the transverse component of the force is considered, since the longitudinal component evaluates to zero when integrated over the symmetric integrand. The corresponding energy transfer is given by:

$$\Delta E(b) = \frac{(\Delta p)^2}{2m_e} = \frac{2Z^2e^4}{(4\pi\epsilon_0)^2 m_e v_r^2 b^2} \tag{2.3}$$

So far only a single collision was considered, which will now be extended to the ion undergoing multiple scatterings. This is described by the statistically averaged variance of the momentum components, transferred over the collision planes at a fixed impact parameter

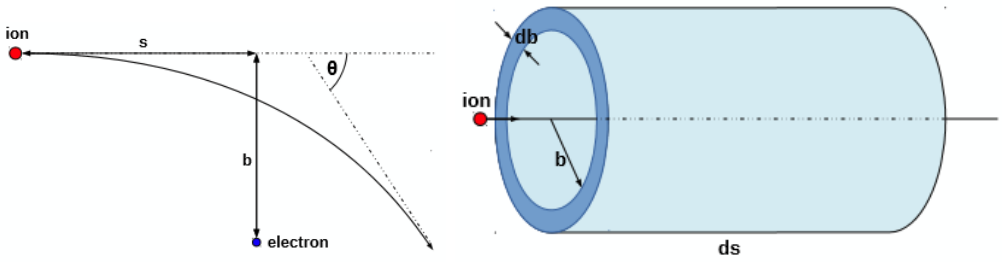

(a) (b)

Figure 2.2: Kinematic collision geometry in the electron beam rest frame. Panel a): Scattering of positive ion from negative electron with scattering angle θ and impact parameter b. Panel b): Illustration of the integration over possible impact parameters b for an ion passing the electrons in their rest frame. Figures are taken from Wilhelm 2019.

b:

$$\langle \Delta p_m \Delta p_n \rangle = \frac{1}{2} \left(\delta_{mn} - v_{r_m} v_{r_n} / v_r^2 \right) (\Delta p)^2 = \left(\delta_{mn} - v_{r_m} v_{r_n} / v_r^2 \right) \frac{2 Z^2 e^4}{(4\pi\epsilon_0)^2 v_r^2 b^2} \tag{2.4}$$

where m and n describe the coordinates of v. Using these last two equations, the cooling force and the so called diffusion tensor can be obtained assuming a mono-energetic electron beam:

$$\vec{F}_{\text{cool}} = -2\pi \int_0^\infty n_\text{e} b \Delta E(b) \frac{\vec{v_r}}{v_r} db = \frac{4\pi Z^2 e^4 n_\text{e}}{(4\pi\epsilon_0)^2 m_\text{e}} \frac{\vec{v_r}}{v_r^3} \int_0^\infty \frac{db}{b} \tag{2.5}$$

$$\begin{aligned} D_{mn} = \frac{\langle \Delta v_m \Delta v_n \rangle}{\Delta t} &= \frac{1}{m_\text{i}^2} \int_0^\infty 2\pi n_\text{e} b v_r \langle \Delta p_m \Delta p_n \rangle \, db \\ &= \frac{2\pi n_\text{e}}{m_\text{i}^2} \frac{2 Z^2 e^4}{(4\pi\epsilon_0)^2} \left(\frac{\delta_{mn}}{v_r} - \frac{v_{r_m} v_{r_n}}{v_r^3} \right) \int_0^\infty \frac{db}{b} \end{aligned} \tag{2.6}$$

The cooling force describes the average particle velocity change and the diffusion tensor the increase of the velocity variance. They are related by the following equation:

$$F_{\text{cool},n} = \frac{1}{2 m_\text{e}} \frac{\partial D_{mn}}{\partial v_{r_m}} \tag{2.7}$$

The integral over the impact parameters diverges and is therefore replaced by the so called *Coulomb logarithm* L_C:

$$\int_0^\infty \frac{db}{b} \longrightarrow \int_{b_\text{min}}^{b_\text{max}} \frac{db}{b} = \ln \left(\frac{b_\text{max}}{b_\text{min}} \right) = L_C \tag{2.8}$$

where b_max and b_min are the maximum and minimum impact parameters respectively, which are used as integration limits. The minimum impact parameter can be obtained by

considering a collision with the maximum possible momentum transfer:

$$\frac{2Ze^2}{4\pi\epsilon_0 v_r b_{\min}} = 2m_e v_r \rightarrow b_{\min} = \frac{Ze^2}{4\pi\epsilon_0 m_e v_r^2} \tag{2.9}$$

In the case where v_r is smaller than the thermal velocity spread $\Delta_{e\perp}$ of the electrons, the relative velocity is replaced with $\Delta_{e\perp}$. The transverse velocity spread is used since it is typically larger than the longitudinal velocity spread $\Delta_{e\parallel}$. The two velocity spreads are given by:

$$\Delta_{e\parallel} = \sqrt{k_B T_{e\parallel}/m_e} \tag{2.10}$$

$$\Delta_{e\perp} = \sqrt{2k_B T_{e\perp}/m_e} \tag{2.11}$$

A reasonable estimate for the maximum impact parameter is the Debye screening length $\lambda_\perp = \sqrt{\epsilon_0 k_B T_\perp/(n_e e^2)}$ of an ion in the electron plasma. However this screening length can be bigger for an ion moving with relative velocity v_r and is then given by v_r/ω_{pl} with the plasma frequency $\omega_{\text{pl}} = \sqrt{n_e e^2/\epsilon_0 m_e}$ as described in Beutelspacher 2000. Therefore both impact parameters are given by:

$$b_{\max} = \max(v_r/\omega_{\text{pl}}, \lambda_\perp) \tag{2.12}$$

$$b_{\min} = \frac{Ze^2}{4\pi\epsilon_0 m_e}\frac{1}{\max(v_r, \Delta_{e\perp})^2} \tag{2.13}$$

The cooling force then becomes:

$$\vec{F}_{\text{cool}} = -\frac{Z^2 e^4 n_e}{4\pi\epsilon_0^2 m_e}\frac{\vec{v_r}}{v_r^3} L_C \tag{2.14}$$

The last aspect to consider is the velocity distribution $f(\vec{v_e})$ of the electrons. Thus, the relative velocity v_r is replaced with $\vec{v_r} = \vec{v_i} - \vec{v_e}$ and the cooling force is integrated over all possible electron velocities:

$$\vec{F}_{\text{cool}}(\vec{v_i}) = -\frac{Z^2 e^4 n_e}{4\pi\epsilon_0^2 m_e}\int L_C f(\vec{v_e})\frac{\vec{v_i} - \vec{v_e}}{|\vec{v_i} - \vec{v_e}|^3} d^3\vec{v}_e \tag{2.15}$$

The velocities of the electron beam produced by an electron cooler typically follow a flattened Maxwellian distribution (Wilhelm 2019) with the average velocity $\langle v_{e\parallel}\rangle$:

$$\begin{aligned} f(\vec{v_e}) &= \left(\frac{m_e}{2k_B T_{e\perp}}\sqrt{\frac{m_e}{2k_B T_{e\parallel}}}\frac{1}{\pi^{3/2}}\right) e^{-\frac{m_e}{2k_b}\left(\frac{v_{e\perp}^2}{T_{e\perp}} + \frac{\left(v_{e\parallel} - \langle v_{e\parallel}\rangle\right)^2}{T_{e\parallel}}\right)} \\ &= \frac{1}{\Delta_{e\perp}^2\sqrt{2}\Delta_{e\parallel}\pi^{\frac{3}{2}}} e^{-\left(\frac{v_\perp^2}{\Delta_{e\perp}^2} + \frac{\left(v_{e\parallel} - \langle v_{e\parallel}\rangle\right)^2}{2\Delta_{e\parallel}^2}\right)} \end{aligned} \tag{2.16}$$

Inserting this distribution into equation 2.15, the cooling force can be calculated numerically. For this thesis, only the longitudinal component is relevant, which is calculated using cylindrical coordinates and the substitution $v_{e\parallel} \rightarrow v_{e\parallel} + \langle v_{e\parallel}\rangle$ to get the cooling

force as a function of the relative velocity $v_r' = v_{i\parallel} - \langle v_{e\parallel} \rangle$ between the longitudinal ion velocity and the average electron velocity. Now equations 2.15 and 2.16 can be evaluated to:

$$F_\parallel(v_r') = -\frac{Z^2 e^4 n_\mathrm{e}}{4\pi\epsilon_0^2 m_\mathrm{e}} \int_0^{2\pi} \int_{-5\Delta_{e\parallel}}^{5\Delta_{e\parallel}} \int_0^{5\Delta_{e\perp}} L_C f(\vec{v}_e) \frac{v_r' - v_{e\parallel}}{\sqrt{\left(v_r' - v_{e\parallel}\right)^2 + v_{e\perp}^2}^3} v_{e\perp} \cdot d\phi dv_{e\parallel} dv_{e\perp} \tag{2.17}$$

$$f(\vec{v}_e) = \frac{1}{\Delta_{e\perp}^2 \sqrt{2} \Delta_{e\parallel} \pi^{\frac{3}{2}}} e^{-\left(\frac{v_{e\perp}^2}{\Delta_{e\perp}^2} + \frac{v_{e\parallel}^2}{2\Delta_{e\parallel}^2}\right)} \tag{2.18}$$

Here the assumption $v_{i\perp} << v_{e\perp}$ was made and $v_{i\perp}$ was therefore neglected in the calculation of $|\vec{v_i} - \vec{v_e}|$. The integration limits were chosen to be five times the velocity spread of the distribution because the value of the integral outside these limits evaluates to less than $6 \cdot 10^{-7}$. The results of the numerical integration for different ion species are discussed in chapter 4.4.

The longitudinal cooling force based on this model qualitatively looks like it is shown in Figure 2.1 b). For small deviations of the ion and electron velocity the cooling force is linear, because the denominator in the integral in equation 2.17 is dominated by the electron velocity components leaving the linear dependence on v_r' in the numerator. The maximum and minimum of the cooling force curve depends largely on the longitudinal velocity spread of the electrons $\Delta_{e\parallel}$, whereas the transverse velocity spread $\Delta_{e\perp}$ mostly affects the scale of the entire curve. For velocity differences past the extreme points the cooling force converges back towards zero with a $\frac{1}{(v_r')^2}$ dependence. This is due to the fact that now the relative velocity v_r' is larger than the electron velocity components. Neglecting the latter results in a dependence of $\frac{v_r'}{(v_r')^3} = \frac{1}{(v_r')^2}$.

As mentioned in the beginning of the section, the previously derived cooling force of the binary collision model can be extended by effects of a solenoidal magnetic field. In such a magnetic binary collision model, the magnetic field causes the electrons to gyrate around the field lines with the cyclotron frequency $\omega_{e,c} = \frac{eB}{m_\mathrm{e}}$. Two types of collisions are distinguished based on the average electron-ion collision time, fast or non-magnetic collisions and adiabatic collisions. In adiabatic collisions the electrons complete many gyrations within the collision time and their transverse velocity in a single collision averages to zero. The influence of the magnetic field also changes the range of possible impact parameters. This increases the cooling force, meaning it is expected to observe larger cooling forces than predicted by equations 2.17 and 2.18. This magnetic model was not used in this thesis because there are issues with the possible impact parameters. The two ranges of magnetic and non-magnetic impact parameters are not connected for some velocity differences leading to a gap of impact parameters between the maximum non-magnetic on and the minimum magnetic one that are not considered. This however is not realistic, which is why the non-magnetic model was chosen.

2.3. Cooling force Measurement Method

Optimising the cooling force is important to get the best possible ion beam quality for collision experiments. This requires quantitative measurements of the cooling force curve. There is no direct experimental access to the cooling force, but there exist indirect measurement methods (Danared 1997). One of those is the voltage step method where the electron and ion velocity is matched before the electron energy is changed rapidly, accelerating the ions. This acceleration is measured and converted into the cooling force. This method however is only feasible for relative velocities above about $10\,000\,\frac{\mathrm{m}}{\mathrm{s}}$, which limits its use.

Another method described by Danared 1997 is based on the phase between a RF-bunching signal and the signal induced in an electrostatic pickup by the passing ion bunches. The electron energy is rapidly adjusted to a different value, changing the phase between the two signals. Now the phase difference between before and after the energy jump is used to calculate the cooling force. Therefore it will be referred to as the phase shift method. This measurement method was used to record the data presented in this thesis because it can be used to map the entire range of relative velocities.

Bunching is the process of dividing a constant stream of ions into several packages called bunches, where the ion density is increased. A more detailed description about bunching is given by Wilhelm 2019, whose descriptions will be used here. This measuring method uses a bunched ion beam, which is created with the help of the RF-bunching system of a storage ring. An alternating, time dependent voltage $U_{\mathrm{RF}}(t) = -\hat{U}_{\mathrm{RF}} \cos(\omega_{\mathrm{RF}} t)$ with amplitude $\hat{U}_{\mathrm{RF}}$ is applied on a drift tube of length L. Its frequency is set to an multiple h of the ion beam revolution frequency $\omega_0 = 2\pi f_{\mathrm{rev}}$:

$$\omega_{\mathrm{RF}} = \omega_0 \cdot h \tag{2.19}$$

This integer value h is called the harmonic. The applied voltage accelerates or decelerates ions based on the time they entered the drift tube. The energy gained by an ion passing the drift tube is given by:

$$\Delta E_{\mathrm{RF}} = Ze\hat{U}_{\mathrm{RF}} \left[\cos(\Phi - \omega_{\mathrm{RF}} t_f) - \cos(\Phi + \omega_{\mathrm{RF}} t_f)\right] \tag{2.20}$$

where $\Phi = \omega_{\mathrm{RF}} t$ is the phase of the RF-signal when the ion is in the center of the drift tube and $t_f = \frac{L}{2v_0}$ is the time it takes the ion to pass half the drift tube at a speed v_0. Therefore the first cosine represents the RF voltage when the ion enters the tube and the second describes the situation when it leaves the tube. The difference in voltages ΔU shown in Figure 2.3 a) multiplied by the ion charge results in an energy gain or loss. Using the following trigonometric identity:

$$\cos(x \pm y) = \cos(x)\cos(y) \mp \sin(x)\sin(y) \tag{2.21}$$

and

$$\omega_{\mathrm{RF}} \cdot t_f = h 2\pi f_{\mathrm{rev}} \frac{L}{2v_0} = h\pi \frac{v_0}{C_0} \frac{L}{v_0} = h\pi \frac{L}{C_0} \tag{2.22}$$

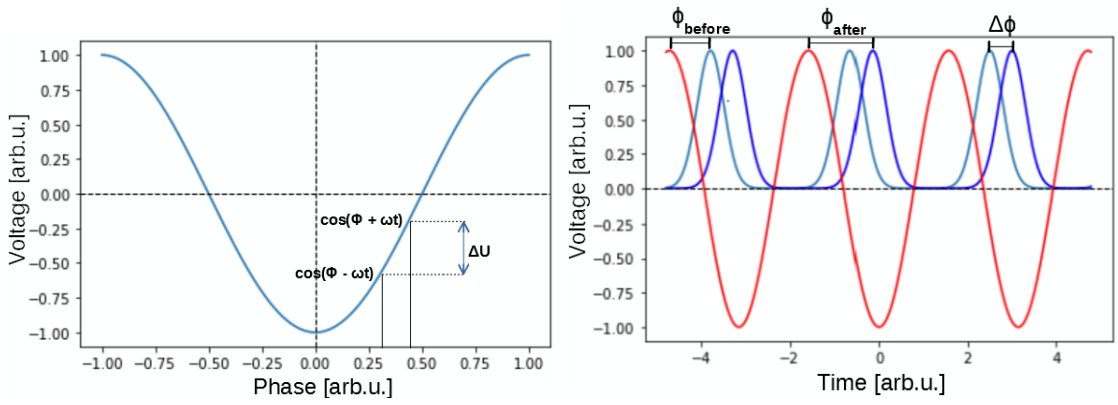

(a) (b)

Figure 2.3: Panel a): RF signal and voltage difference ΔU. Panel b): phase ϕ_{before} and ϕ_{after} between bunching (red) and pickup signal before (light blue) and after (dark blue) the jump in electron energy resulting in a phase difference $\Delta\phi$.

equation 2.20 can be rewritten as:

$$\Delta E_{\text{RF}} = Ze\hat{U}_{\text{eff}} \sin(\Phi) \tag{2.23}$$

with

$$\hat{U}_{\text{eff}} = 2\hat{U}_{\text{RF}} \sin\left(h\pi \frac{L_0}{C_0}\right) \tag{2.24}$$

The energy change of the ions based on the phase of the RF signal accelerates ions that arrive when the voltage is positive and slows down ions that enter the drift tube while the voltage is negative. This effect pushes ions together and creates an ion bunch. In every bunch there is a *synchronous* particle that always enters the drift tube with the same RF phase being present. Neglecting any collision effects in-between the ions this phase would be zero, meaning the particle neither gains nor loses energy during a revolution. In the case of the other ions the phase is not the same when they arrive at the RF system and they are therefore accelerated or decelerated, which causes synchrotron oscillations around the synchronous particle to occur. Since the RF frequency is h times larger than the revolution frequency, h bunches can be created.

The phase shift measurement method requires the RF voltage but also ion beam diagnostics by a current pickup. This pickup detects mirror charges induced by passing charged particles and is described in more detail in section 3.1. In the case of a bunched ion beam, this signal consists of short pulses created by passing ion bunches as shown in Figure 2.3 b).

Such a bunched ion beam can be used to measure the cooling force as mentioned in the beginning of this section. Such a measurement is initiated by matching the velocities of electrons and ions. Now the ions do not lose any energy in the electron cooler and there is an arbitrary and constant phase between the RF signal and the pickup signal. Now the

electron energy is, for example, suddenly reduced, which means that the ion beam now loses energy in each revolution. This causes the bunching phase to shift until the energy loss is compensated by the RF-system. This phase shift is what is being recorded. Using the difference in phase $\Delta\phi = \phi_{\text{after}} - \phi_{\text{before}}$ before and after the electron energy change, the energy that is now being lost in the cooler can be calculated:

$$\Delta E_{\text{RF}} = Ze\hat{U}_{\text{eff}} \sin(\Delta\phi) \tag{2.25}$$

Dividing the energy by the length l of the electron cooling section results in the equation for the longitudinal cooling force:

$$F_{\parallel} = -\frac{\Delta E_{\text{RF}}}{l} = -Ze\hat{U}_{\text{eff}} \sin(\Delta\phi)/l \tag{2.26}$$

Before the change in electron energy, the average velocities of ions and electrons were matched but after the change they are different. This difference in velocity is called the detuning velocity v_{det} given by

$$v_{\text{det}} = \sqrt{2/m_{\text{e}}} \left(\sqrt{E_{\text{lab}}} - \sqrt{E_{\text{cool}}} \right) \tag{2.27}$$

where E_{lab} is the electron laboratory frame energy after the change and E_{cool} is the electron laboratory frame energy while the velocities are matched. The detuning velocity is the same as the relative velocity v_r' described in section 2.2. The cooling force can be calculated from the phase shift for each detuning velocity to generate the entire cooling force curve.

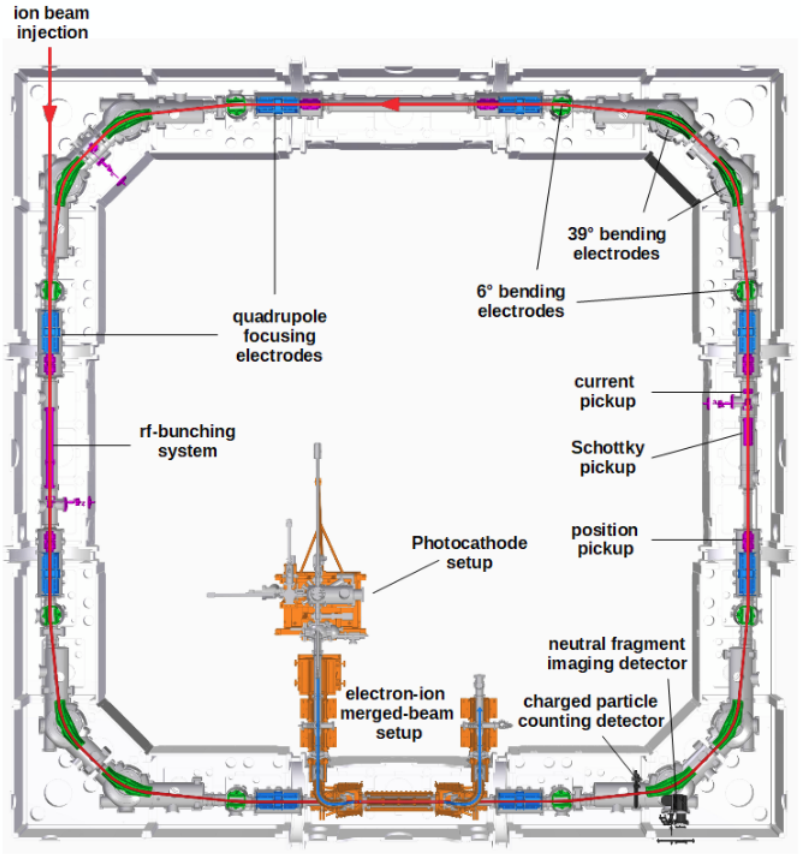

Figure 3.1: Schematic setup of CSR. Figure taken from Wilhelm 2019.

3. Cryogenic Storage Ring (CSR)

The measurements presented in this thesis were conducted at the electrostatic cryogenic storage ring (CSR) at the Max-Planck-Institut für Kernphysik in Heidelberg, which is described by von Hahn *et al.* 2016. In this section a short overview of the storage ring will be given followed by a description of the electron cooling system.

3.1. Overview of the Ring

The symmetric electrostatic storage ring CSR has a circumference of 35.12 m and consists of four straight sections as shown in Figure 3.1. To guide the beam through the ring electric fields created by two 6° minor deflectors and two 39° major deflectors in each corner are used and electric fields produced by electrostatic quadrupole electrodes focus the ion beam. The walls of the vacuum chamber through which the ion beam travels can be cooled down to temperatures of $\approx 6\,\mathrm{K}$ using a liquid helium refrigerator system. There an extremely low pressures with a corresponding particle density on the order of $\sim 1000\,\frac{1}{\mathrm{cm}^3}$ can be achieved, allowing for ion storage times of several tens of minutes.

Various ion sources are available, that can be attached to one of two high-voltage plat-

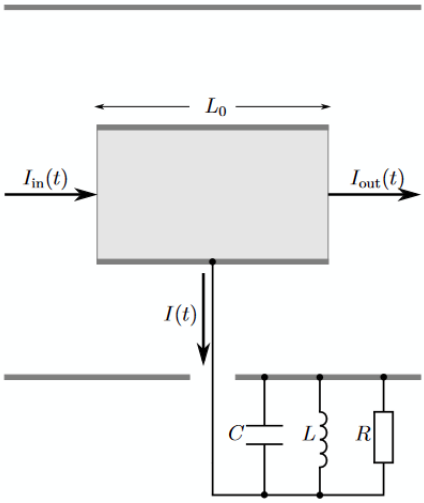

Figure 3.2: Principle of capacitive pickup using Schottky pickup as an example. Ion beam with current $I_{in}(t)$ travels trough pickup with length L_0 inducing a charges on the pickup surface and thus causing a current $I(t)$. This current is interpreted using a resistor with resistance R, a coil with inductance L and a capacitor with capacitance C. Figure taken from Vogel 2016

forms with upper acceleration voltage limits of 60 kV and 300 kV. Therefore particles with up to 300 keV kinetic energy per unit charge can be stored in the ring.

The four straight sections of the ring are dedicated to experiments and beam diagnostics. One of those sections is purely used for ion beam diagnostics. A detailed description of all of these elements has been done by Vogel 2016. It contains different types of capacitive pick-ups. Their basic principle is based on the detection of mirror charges induced by an ion beam with current I_{in}. They consist of a hollow tube of length L_0, through which the particles move and where the mirror charges are created. This results in a current that can be measured and interpreted by a combination of resistors, coils and capacitors. This enables the detection of ion density variations within one revolution of the beam such as in a bunched ion beam. Based on the specific pickup, different information about the ion beam can be gained in a non-destructive manner, such as the ion number and current with a current pickup. The Schottky pickup is typically used to detect Schottky noise in a coasting beam and the position pickup can determine the transverse beam position.

Another sections contains the RF-bunching system, which uses a radio-frequency (RF) voltage to divide the ion beam into bunches as described in section 2.3. This increases the detection sensitivity by pickup electrodes and in some cases a bunched beam is necessary for a certain measurement like the cooling force measurement method discussed previously.

A third section of the ring is used not only for ion photon collision experiments but also merged beam experiments with the help of the electron cooler, marked in orange in Figure 3.1. The electron cooler provides an electron beam that can apply phase space cooling to

the ion beam as well as act as a high-resolution collision target. It will be explained in more detail in section 3.2.

In order to detect and analyze particles resulting from ion collisions two multi-channel plate (MCP) detector systems have been installed. They are located behind the first 6° deflector downstream of the electron cooler, which means the collision products are separated due to their different charge-to-mass ratio compared to the ion beam. One of the two detectors is the Cold Movable Particle Counter (COMPACT), described by Spruck *et al.* 2014, which is a movable, cryogenic, single particle detector capable of detecting charged and neutral particles that specializes in studying reactions with low cross sections due to its low dark count rate as well as its high detection efficiency. The other detector is the Neutral particle Imaging in Cold Environment (NICE) detector used in the position imaging of neutral fragments with a high time resolution. More information about this detector is given by Becker 2016.

3.2. Electron Cooler

In this section the design (see Shornikov 2012) of the electron cooler shown in Figure 3.3 is described using information given by Paul 2021.

In the electron gun of the electron cooler electrons are produced using the photoelectric effect. A GaAs photocathode with negative electron affinity is illuminated by a laser creating free electrons with a quantum efficiency between 8 - 20 %. Throughout the entire electron cooler the electron beam is guided by magnetic fields.

The electrons are extracted through a 3 mm aperture of the Pierce shield at the potential U_{pierce} compared to the cathode potential U_0. The extraction electrode at a higher potential U_{ext} relative to the cathode is used to accelerate the electrons. Next, the electron beam leaves the high magnetic field B_{gun} in the the electron gun and enters the lower magnetic field produced by three solenoids. This leads to an expansion of the electron beam by the so called expansion factor

$$\alpha = \frac{B_{\text{gun}}}{B} \tag{3.1}$$

in a section with magnetic field B. The beam is expanded again when entering the interaction region. An expanded electron beam has an increased diameter and a lower transverse temperature but the electron density is decreased. The beam radius scales with $\sqrt{\alpha}$, the transverse temperature with $\frac{1}{\alpha}$ and the density with $\frac{1}{\alpha}$.

Following the room temperature solenoids the beam is bent by 90° in the horizontal plane and by 30° in the vertical plane by the toroidal solenoid. Then it is merged with the ion beam using a dipole field created by the merging coils. This field also affects the ion beam, which is why the ion beam is bent slightly using the correction coils prior to being merged with the electron beam. A symmetrically identical setup is used to separate the two beams again after the interaction region.

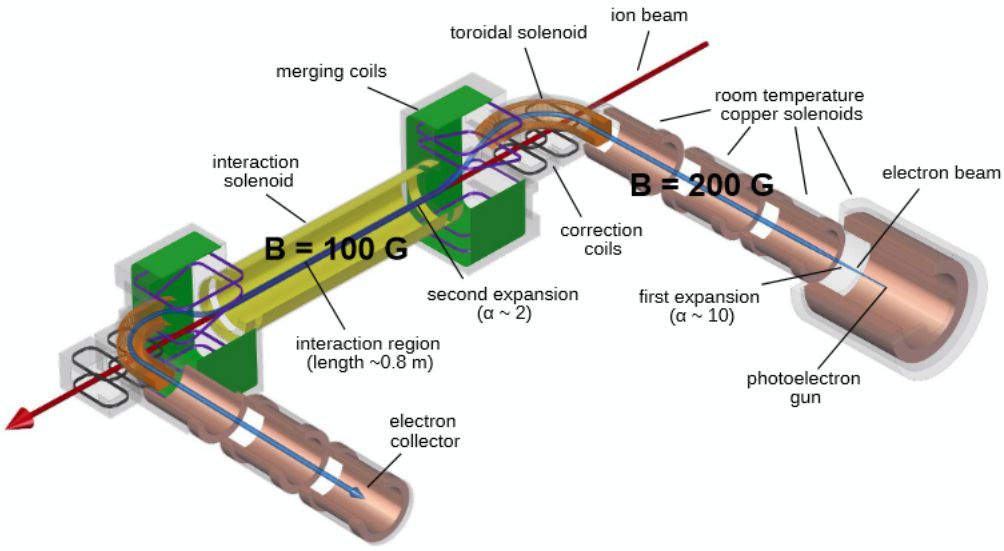

Figure 3.3: Schematic model of the CSR electron cooler. Figure taken from Paul 2021.

In the interaction region, with a length of $\approx 0.8\,\mathrm{m}$, the second expansion of the beam happens. Here the electron beam passes through a drift tube, which is at a potential U_{int} with respect to to the cathode and sets the electron energy to the desired value. This interaction voltage is defined by a power supply, that creates a voltage between the photocathode and the drift tube. This voltage can be changed quickly on a millisecond timescale to switch between the electron cooling energy and the detuned electron collision energy needed in an experiment.

Then the electron beam is de-merged and hits the electron collector after passing through more solenoids. Here the electrons are collected by a Faraday cup with a small pinhole through which some electrons can pass and hit an analyser cup. This enables electron beam profile measurements.

In order to achieve the best possible overlap of the electron beam with the ion beam it is necessary to be able to change the beam position and angle in the interaction region. This is achieved by steering coils located in different sections of the electron cooler. All magnetic fields in the cryogenic region of the cooler are generated by coils made of High-Temperature Superconductor material, that needs to be cooled using a closed-cycle helium or neon cooling system on top of the electron cooler.

For the applications demonstrated in this thesis, a typical electron beam produced by this setup had a radius r_{e} between 5 and 7 mm in the interaction zone, a current I_{e} between 5 - 10 μA with an electron density n_{e} between 1 - 10 $\frac{10^5}{\mathrm{cm}^{-3}}$. The value of the longitudinal temperature $k_B T_{e\parallel}$ usually lied between 100 and 250 μeV and the one of the transverse temperature $k_B T_{e\perp}$ at around 2.25 meV.

4. Cooling force measurement and data analysis

This chapter is about the cooling force measurements conducted at CSR using the measurement method described in section 2.3 and the obtained results. It starts with a description of the measurement procedure and setup in section 4.1. Then follows section 4.2, which is about the evaluation methods of the recorded data of the four different ions, Xe^{3+}, ArH^+, HeH^+ and Ne^{2+} and the individual approach to each of them. In section 4.3 the systematic effects, that various settings have on the resulting cooling force curves, are analysed. Afterwards, in section 4.4, the theoretical model from section 2.2 is compared with the experimental results.

4.1. Measurement setup and procedure

The measurement requires two voltage signals, the applied RF bunching voltages and the current pickup signal. Both signals are transferred to a SR860 500 kHz DSP Lock-in Amplifier, which can determine the phase between these two signals. More information about lock-in amplifiers can be found here[1]. The various settings that were used for the measurements of the different data sets are found in table 4.1. The lock-in data can be accessed using an USB stick and saved manually with the press of a button. Since this is tedious and unreliable, a recording software was developed in the course of this thesis to control the lock-in amplifier remotely via the VXI-11 protocol and thus automate the data collection process. It can be used to set the most important lock-in settings and it writes the phase and the time since the start of recording into a file as described in more detail in appendix A.

The measurement starts by injecting a new ion beam into the ring, followed by bunching as well as electron cooling for a certain amount of time. After enough time has passed to reach a stable pickup signal, the electron energy is changed rapidly to the new value, which is done using another software. The recording software is synchronized with the ion storage time and starts collecting between 5 and 15 s before the jump and stops between 2 and 5 s after the jump. Then the beam is kicked out of the ring, new ions are injected, and the process repeats with a different change in electron energy this time. This process continues until all desired energy jumps, between 25 and 40 in this case, have been recorded. Since the development of the recording software all of this is coordinated using computer programs, allowing for quick cooling force measurements.

This however was not the case for the first two measurements with ArH^+ and HeH^+

[1] https://www.thinksrs.com/downloads/pdfs/applicationnotes/AboutLIAs.pdf

Ion	Time constant	Sensitivity	Input range	Recording time [s]	Sampling interval
Xe^{3+}	0.3 ms	100 mV	300 mV	35	$\sim$ 0.8 ms
HeH^+	1 ms	50 mV	100 mV	10	$\sim$ 15.6 ms
ArH^+	1 ms	50 mV	100 mV	10	$\sim$ 15.6 ms
Ne^{2+}	0.3 ms	100 mV	300 mV	7	$\sim$ 0.4 ms

Table 4.1: Lock-in amplifier settings for the different data sets.

ion beams. Here the data had to be saved to an USB stick, which also had the effect, that the possible time resolution was much worse compared to the automated recording method. Therefore, the ArH^+ and HeH^+ data of one jump consists of only 640 data points representing a time frame of 10 s and leading to a time resolution of about 15.6 ms. For the other two ions the data were recorded automatically. This method was able to record data with a resolution of about 0.4 ms over a time span of 7 s in the case of Ne^{2+} or a resolution of about 0.8 ms over a duration of 35 s in the case of Xe^{3+}.

4.2. Evaluation of Data

In this section the different approaches to evaluating the data of the ions are presented. Due to the different quality of data for each ion species, they need to be handled differently. The manually recorded data have the issue that the jump does not happen at the same time within the recording for each jump, since it is not time-synchronized with the energy change of the electrons through software. This means that the jump time within the recording needs to determined manually for each jump instead of being the same every time like it is the case with the automatically recorded data. This is not only more work but also increases the effect of human error. Another difference is the time resolution, which reveals certain effects in the high resolution data, while they can not be seen with the low resolution.

Evaluating data means calculating the phase jump for each recording by subtracting the phase before the jump from the phase after $\Delta\phi = \phi_{\text{after}} - \phi_{\text{before}}$, where the absolute value of ϕ_{before} is caused by delays in the electronic systems and as a result is arbitrary. Determining these two points is not as straight forward as one might think. Unlike the theory, described in section 2.3, which assumes a simple phase step after the changes in electron energy, the real phase development is not constant after the jump. In the acquired lock-in graphs the phase jumps are not instant and take a certain amount of time. Also in some cases the phase rises continuously and never reaches a steady value. This is probably due to non-linear effects that are not taken into account by the simplified model of the cooling force measurement. Therefore, there is room for interpretation as to where the "end" of the jump is and the individual approach to determining the phase shift for each ion species is presented in the next section. This value is then used to calculate the cooling force according to equation 2.26.

It starts with the Xe^{3+} data since it has been recorded last with better settings than for the previously recorded ions and as a consequence it is the easiest to interpret. Then the two manually recorded data sets of ArH^+ and HeH^+ will be shown and evaluated, followed by Ne^{2+}.

4.2.1. Xe^{3+} data

This measurement consists of two runs with 29 phase jumps each. The ion beam was injected and cooled for 50 s before the bunching started. The recording began 40 s after that and the jump happened 15 s into the recording. After another 15 s the electron energy was changed back to the initial value and the phase jumped back. A typical result of this can be seen in Figure 4.1 a). In this case the electron energy was changed from the cooling

energy of $E_{\text{cool}} = 3.819\,\text{eV}$ to $3.7838\,\text{eV}$ resulting in a detuning velocity of about $-5300\,\frac{\text{m}}{\text{s}}$.

Various methods for determining the phase shifts $\Delta\phi$ are compared in Figure 4.1 for one specific example of an electron energy jump. One possibility is shown in Figure 4.1 b) and c) where the time of the jump was known and an arbitrary model function was fitted through the points before and after the jump. The points at the jump are marked with red dots and are used to calculate the size of the phase jump $\Delta\phi$. As a fit function a linear function (panel c)) and a second degree polynomial (panel b)) were used and compared. In general the polynomial function is a better model of the data.

Another option is to apply a rolling average, where the average value of a defined number of neighbouring points is calculated and then attributed to the time of the point in the center of the averaging range. This is shown in Figure 4.1 e) and f). As the ϕ_{before} value the latest rolling-average point before the jump is used, that is not yet including the data after the jump. E.g. for a rolling average over 100 points and a sampling time of about 0.8 ms this point is about 40 ms before to the jump. For the phase value after the jump ϕ_{after} a similar approach is used, the difference here is that the point that comes 0.3 s after the jump is used. The examples show a rolling average over 100 and 500 data points, which represent $\sim 0.08\,\text{s}$ and $\sim 0.4\,\text{s}$ respectively. For the rest of the Xe^{3+} analysis discussed below, the average over 500 points is used.

Applying one of these methods to all jumps in a run and determining the corresponding cooling force for each detuning velocity creates a cooling force curve shown in Figure 4.2 a). The different ways of analysing the jumps are used to estimate the systematic error introduced by the analysis. The main point is the average value of the maximum and minimum point out of the three points determined using the the three methods and the errorbars extend to the maximum and minimum value as shown in Figure 4.2 b). For the first run of the two Xe^{3+} runs, run 0136 shown in Figure 4.2, the average size of the error is $\sim 3.2\,\frac{\text{meV}}{\text{m}}$ and the maximum error is $\sim 7.0\,\frac{\text{meV}}{\text{m}}$. Compared to the peak-to-peak value of the curve, $\sim 282.6\,\frac{\text{meV}}{\text{m}}$, this results in an average relative error of about 1.1 %. For the second run with the number 0137 this relative error is 2.2 %.

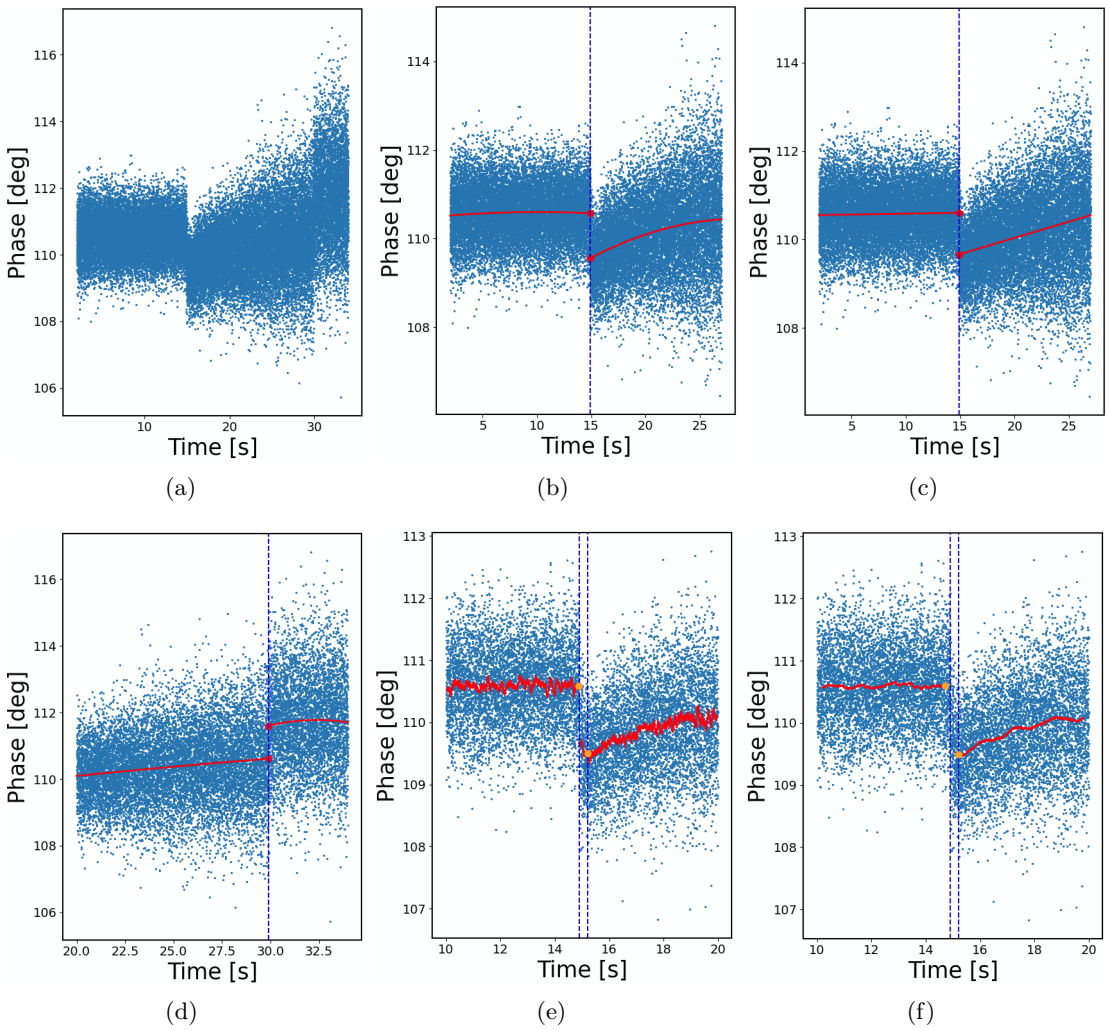

Figure 4.1: Example of Xe^{3+} data and evaluation. All six panels show the same data set but with different time ranges. Physical parameters of this data set are given in the main text. Panel a) shows the raw recorded data of two phase jumps at 15 s and 30 s. In panel b) the dashed line marks the first jump and the red dots determine the jump size which are at the end of the second-order polynomial fit functions through the points before and after the jump. Panel c) is the same as panel b) except the fit function is a linear function. Panel d) is the same as panel b) but with the second jump. Panel e) shows the rolling mean over 100 points. The left dashed line marks the first jump and the second line, 0.3 s past the jump, marks the point in the rolling mean which is used to calculate the jump size. These points are marked with orange dots. Panel f) is the same as panel e) but averaging over 500 points.

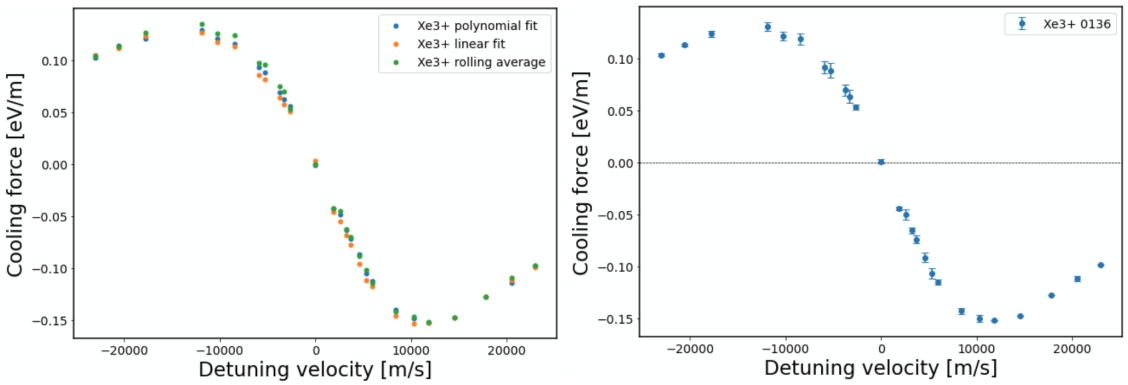

(a) (b)

Figure 4.2: Cooling curves of the first Xe^{3+} run. Panel a): cooling curves with different methods of analysis. Panel b): cooling force curve where the main points are the mean of the extreme points from the different methods. The error bars extend to these extreme points.

4.2.2. ArH^+ data

The first ion with which the cooling force was measured in the course of this bachelor work was ArH^+. Here only one run was recorded with 43 phase jumps and a cooling energy of $E_{\text{cool}} = 4.017\,\text{eV}$. The ion beam was cooled and bunched for 20 s before the electron energy was changed. An example of recorded phase data is shown in Figure 4.3 a) where the detuning velocity was $\sim 14\,700\,\frac{\text{m}}{\text{s}}$ and the difficulty in interpreting this jump is already apparent.

Unlike in the Xe^{3+} jumps, the phase doesn't stay constant after the jumps but it constantly decreases in this example. This could be e.g. due to a loss of ions after the jump as discussed further in section 4.3. Now the question arises where the phase jumps to and how long the process of shifting the beam is expected to take. In theory the change in electron energy happens on a millisecond timescale and the shift itself should be complete on the timescale of few revolutions of the beam ($\lesssim 0.1\,\text{ms}$). The maximum measured phase shift after the jump however is typically reached after several 100 ms. It is unclear if this peak phase should be used for the calculation or a point in the graph much closer to the jump point.

In order to determine the jump size a fit function like for Xe^{3+} was used, unlike for ArH^+ it is a third degree polynomial. The time of the jump was determined manually by visually adjusting the time until it matches the visible phase jump. To account for the uncertainties just mentioned, the fit after the jump only considered points after a chosen time past the jump time. This is shown in Figure 4.3 b) and c) with the first dashed line marking the jump and the second line the time at which the second fit starts. This was done for offset times between 100 ms and 500 ms, where the range of obtained cooling force amplitudes was used to determine the errorbars of the cooling curve in Figure 4.4 b). The

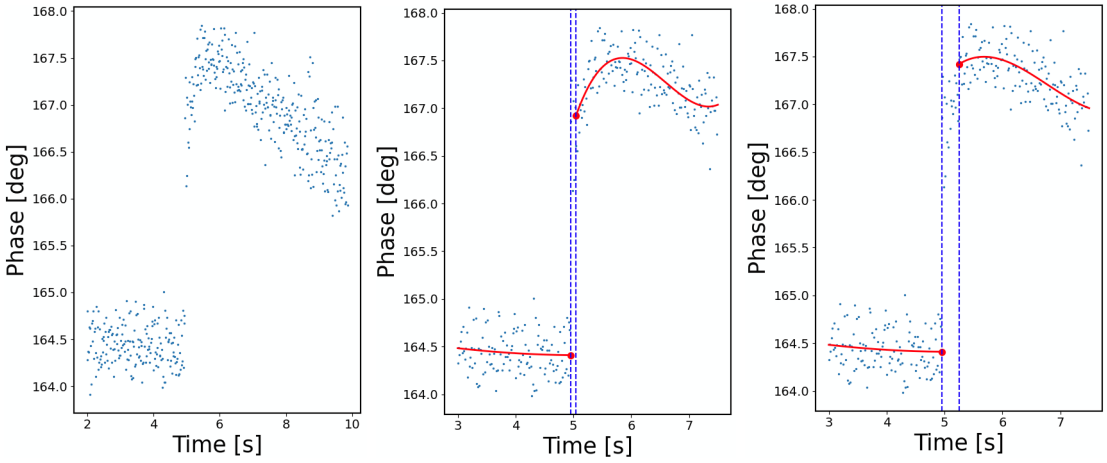

Figure 4.3: Example of ArH^+ data and evaluation. Panel a): raw phase data as a function of recording time. Panel b): First dashed line marks the jump and the second dashed line is 0.1 s after the jump. Only points to the right of it are used in the fit. The red dots at the end of the fits determine the $\Delta\phi$ value. Panel c): same as b) but with a 0.3 s offset after jump.

main point is the mean between the maximum and the minimum point and the errorbars extend from this point to the maximum and minimum.

The largest error here has a value of $\sim 4.6\,\frac{\text{meV}}{\text{m}}$ compared to the average error of $\sim 1.8\,\frac{\text{meV}}{\text{m}}$. The total span of the cooling force curve is $\sim 72.2\,\frac{\text{meV}}{\text{m}}$ and thus the average relative error can be calculated to be 2.5 %. In general there is noticeable difference between the errorbars for positive detuning velocities compared to negative ones. The jumps are much better defined for the negative velocities.

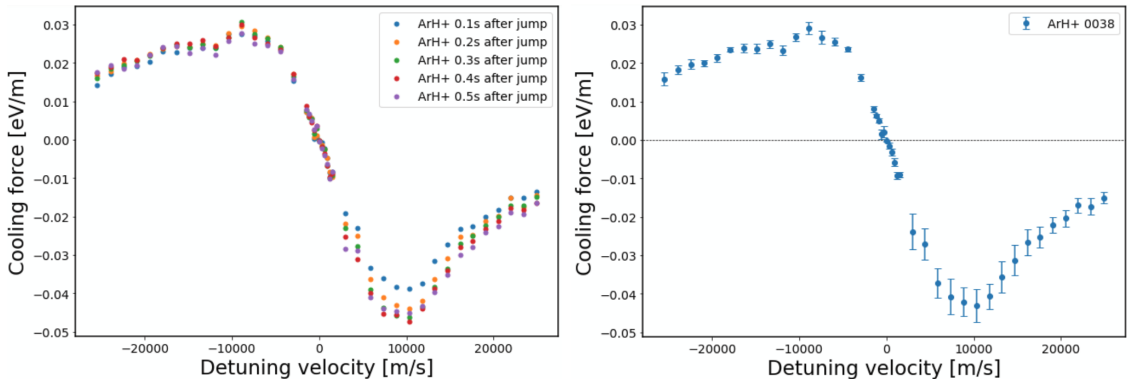

(a) (b)

Figure 4.4: Cooling curves of the ArH^+ run. Panel a): cooling curves with different offset times past the jump. Panel b): cooling curve with error bars based on the different cooling curves in a).

4.2.3. HeH^+ data

The second ion used for cooling force measurements was HeH^+, for which 6 runs were recorded with 27 jumps each and a cooling energy of $E_{\text{cool}} = 9.324\,\text{eV}$. The ion beam was cooled for 3 s before the jump happened. An example of phase data with a detuning velocity of $\sim 3000\,\frac{\text{m}}{\text{s}}$ is shown in Figure 4.5 a).

The jumps are similar to the ArH^+ ones with the same issue of an unstable phase after the jump. Therefore the same technique to determine the $\Delta\phi$ value was applied. Examples of the resulting cooling curves with and without errorbars are shown in Figure 4.6.

In this example of the cooling force curve the average error is $\sim 0.6\,\frac{\text{meV}}{\text{m}}$ and the maximum error is $\sim 1.3\,\frac{\text{meV}}{\text{m}}$. The peak-to-peak value of this curve is $\sim 22.6\,\frac{\text{meV}}{\text{m}}$ leading to an average relative error of 2.6 %. For the other HeH^+ runs this relative error can reach values of up to 5 %. In contrast to the errorbars of the ArH^+ cooling force curve, the HeH^+ curves have more symmetrical errors.

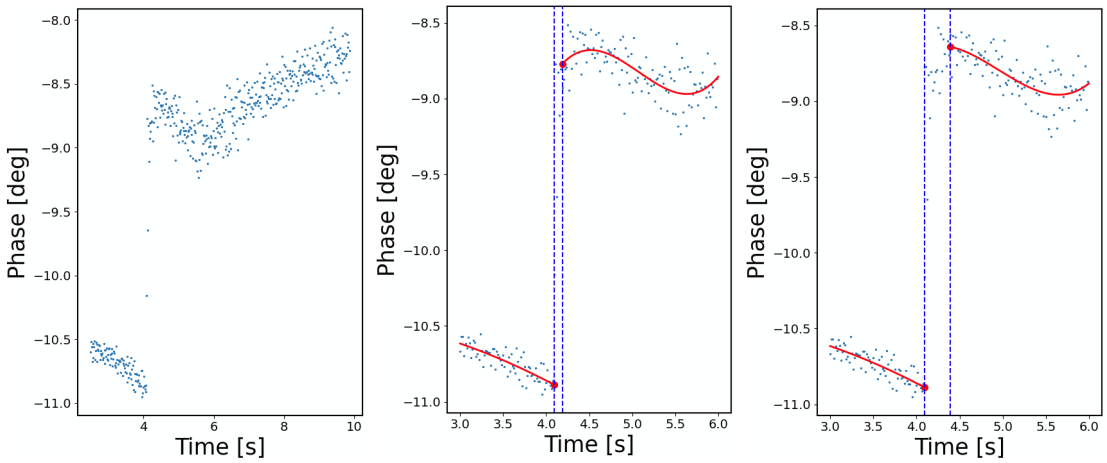

Figure 4.5: Example of HeH^+ data and evaluation. Panel a): raw phase data as a function of recording time. Panel b): First dashed line marks the jump and the second dashed line is 0.1 s after the jump. Only points to the right of it are used in the fit. The red dots at the end of the fits determine the $\Delta\phi$ value. Panel c): same as panel b) but with a 0.3 s offset after jump.

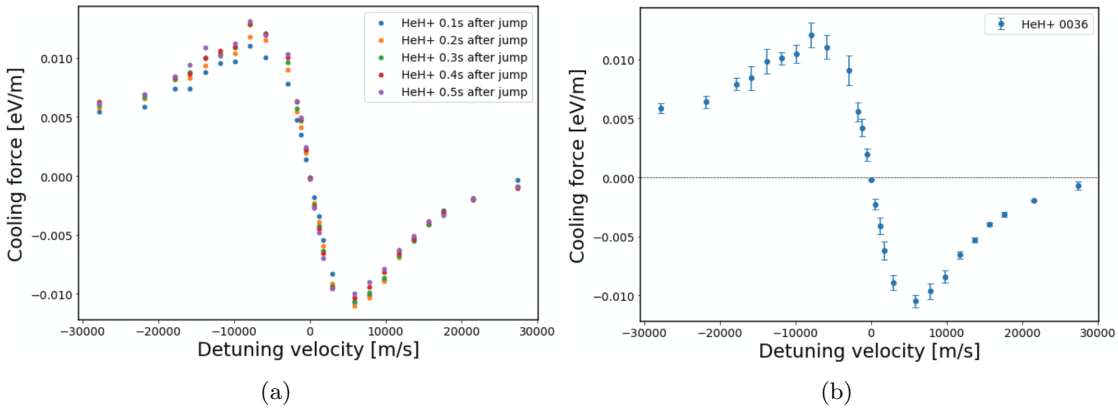

Figure 4.6: Cooling curves of the first HeH^+ run. Panel a): cooling curves with different offset times past the jump. Panel b): cooling curve with error bars based on the different cooling curves shown in panel a).

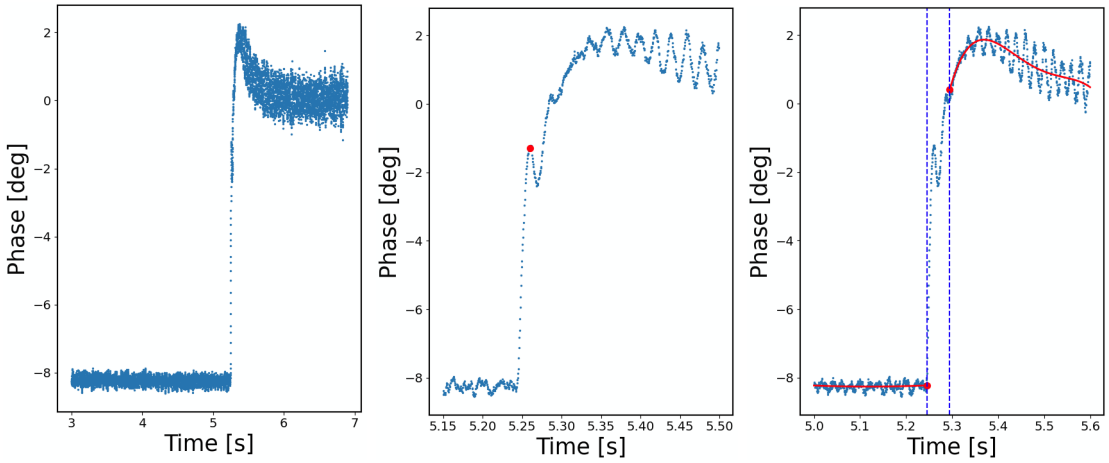

(a) (b) (c)

Figure 4.7: Example of Ne^{2+} data and evaluation. Panel a): raw phase data as a function of recording time. Panel b): zoomed in view of the jump, the red dot marks the first peak, which is also used as ϕ_{after}. Panel c): offset past jump is 0.05 s.

4.2.4. Ne^{2+} data

The final ion is Ne^{2+} with which 3 runs with 47 jumps each were recorded. Here the ion beam was cooled for 5 s before the electron energy was changed from the cooling energy of $E_{\text{cool}} = 16.465\,\text{eV}$ to a different value. An example of a phase jump with a detuning velocity of $\sim 7700\,\frac{\text{m}}{\text{s}}$ and a similar timescale as used for HeH^+ and ArH^+ can be seen in Figure 4.7 a). Next to it is the same jump but zoomed into the time axis and here oscillations during the increase in phase become visible.

For the two previous ions the recording resolution was too small to detect possible oscillations on this timescale. These oscillations occur for every jump and have a similar amplitude every time. Here it is again unclear where the jump ends and where the influence of other effects starts to take over. Thus, not only the method using the fit with different offset times like for the previous two ions was used, but also a direct measurement of the phase at the first peak after the jump, which is then used as the value for ϕ_{after} as shown in Figure 4.8 b). The result for the fit method is shown in Figure 4.8 and the curves using the phase jump to the first peak are shown in the following section in Figure 4.14 a).

With the fit method used for run 0199, the average error has a value of $\sim 17\,\frac{\text{meV}}{\text{m}}$ and the maximum error has a value of $\sim 38\,\frac{\text{meV}}{\text{m}}$. Here the span of the cooling force curve is $\sim 446\,\frac{\text{meV}}{\text{m}}$ and the relative error is therefore 3.8 %.

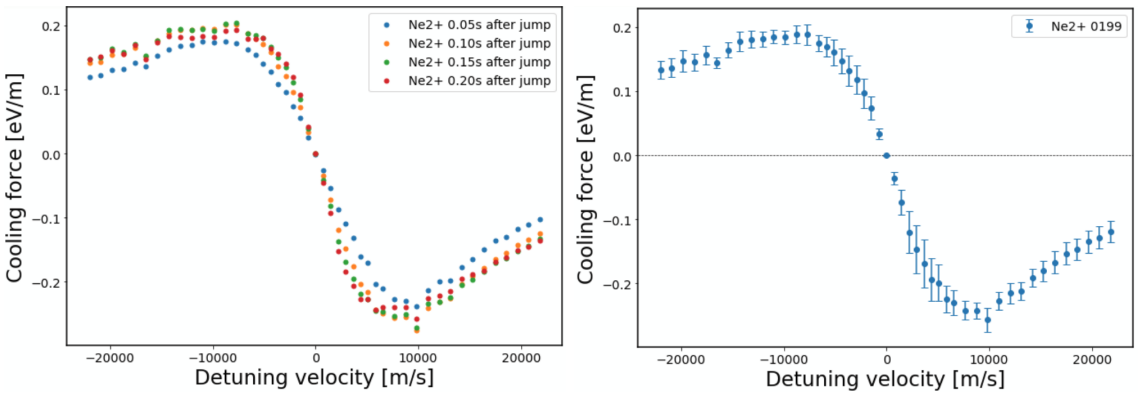

(a) (b)

Figure 4.8: Cooling curves of the first Ne^{2+} run. Panel a): cooling curves with different offset times past the jump. Panel b): cooling curve with error bars based on the different cooling curves shown in panel a).

4.3. Comparison between different Settings

In this section the observed effects of different settings on the cooling force are presented. An overview of all recorded runs with the different ions and the settings can be found in Table 4.2. The settings that were varied are the effective RF bunching voltage, the RF bunching frequency, the ion current, the electron beam position, the cooling time before the jump and the magnetic field in the interaction region.

Influence of the effective bunching voltage

First the effect of the effective bunching voltage on the cooling force will be analysed. This voltage from equation 2.24 can be affected by either changing the amplitude of the RF-voltage or the harmonic number. In theory this parameter should not have any effect on the cooling force since the RF bunching system is independent of the electron cooler. It only affects the size of the phase jumps and with it the data quality. In the Xe^{3+} run 0137 with the larger U_{eff} the largest phase shift was $\lesssim 1°$ compared to the Ne^{2+} run 0199 with a maximum phase shift of $\approx 4°$.

In the measurements done for this thesis the effective bunching voltage was changed between two Xe^{3+}, HeH^+ and Ne^{2+} runs. In the case of HeH^+ the voltage was changed from 0.185 V to 0.367 V between run 0036 and 0038 by doubling the harmonic number from 4 to 8. The two corresponding cooling force curves are shown in Figure 4.9 a). Here an increase in the cooling force amplitude by $\approx 30\%$ is visible with the increase in voltage.

Between the two Xe^{3+} runs 0136 and 0137 the effective bunching voltage was increased from 1.325 V to 2.418 V leading to a decrease in cooling force amplitude by $\approx 15\%$ seen in Figure 4.9 b).

Ion	Run number	Harmonic number	RF frequency [kHz]	Effective RF voltage U_{eff}[V]	Other changes
Xe^{3+}	0136	11	362.800	1.325	-
	0137	11	362.800	2.418	larger U_{eff} vs 0136
ArH^{+}	0038	11	371.850	0.51	-
HeH^{+}	0036	4	206.263	0.185	-
	0038	8	412.526	0.367	larger U_{eff} vs 0036
	0040	8	412.457	0.367	≈15 times lower ion number vs 0038
	0041	8	412.629	0.367	horizontal e-beam shift vs 0040
	0042	8	412.629	0.367	precooling from 3 s to 6 s vs 0041
	0043	8	412.640	0.367	different frequency vs 0038
Ne^{2+}	0199	8	411.270	0.579	-
	0201	8	411.270	2.692	larger U_{eff} vs 0199
	0205	8	411.270	0.579	larger B-field vs 0199

Table 4.2: Parameters of the different ions and runs.

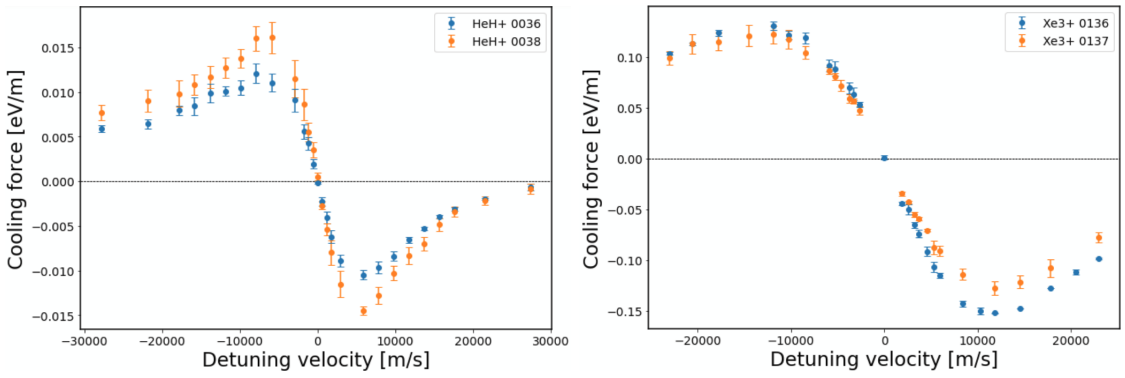

(a) (b)

Figure 4.9: Effect of the effective bunching voltage on the cooling force. Panel a): Comparison between run 0036 and 0038 of HeH^{+}, with bunching voltage increased from 0.185 V to 0.367 V. Panel b): Comparison between run 0136 and 0137 of Xe^{3+}, with bunching voltage increased from 1.325 V to 2.418 V.

Neither of the results is as expected and they both differ in a different direction from the expected result. The effect that the effective bunching voltage has on the cooling force can not be explained yet and could therefore be considered as another systematic error when comparing cooling force curves with different bunching voltages.

In the case of Ne^{2+} this voltage was also changed between run 0199 and run 0205 from 0.579 V to 2.692 V. Here however the recorded data is not usable because even before the jump the phase variance is very large and the jump is negative even in cases where it is expected to be positive, leading to a shifted and uneven cooling force curve.

In general a larger effective bunching voltage leads to smaller phase jumps and increases the errors as seen in Figure 4.9. For effective bunching voltages that are too high and thus leading to very small phase jumps, the measurement method does not seem to work at all.

Influence of the bunching frequency

Next the effect of the bunching frequency will be discussed. The experimental effect can be observed between the HeH^+ runs 0038 and 0043, where nothing but the bunching frequency was changed from 412.526 kHz to 412.640 kHz.

As described in section 2.3 the RF frequency should be an integer multiple of the ion revolution frequency so that the energy of the ion beam on average is affected neither by the RF system nor by the electron cooler before the jump happens. The energy is not changed by the RF system because the synchronous particle enters the drift tube while the RF phase is zero and it is not changed by the electron cooler because the the mean electron and ion velocities are matched.

By changing the RF bunching frequency slightly, while keeping the electron cooling energy, the ion beam now gains and loses energy even before the jump and the synchronous particle reaches the center of the drift tube while the RF signal has a non-zero phase $\phi_{\mathrm{RF,before}} \neq 0$. After the phase jump by $\Delta\phi$ this RF phase is $\phi_{\mathrm{RF,after}} = \phi_{\mathrm{RF,before}} + \Delta\phi$. When the RF and revolution frequency are matched $\phi_{\mathrm{RF,before}} = 0$ and $\phi_{\mathrm{RF,after}} = \Delta\phi$ leading to equation 2.25. Since this is not the case here, this equation changes to

$$\Delta E_{\mathrm{RF}} = Ze\hat{U}_{\mathrm{eff}} \sin(\phi_{\mathrm{RF,after}}) = Ze\hat{U}_{\mathrm{eff}} \sin(\phi_{\mathrm{RF,before}} + \Delta\phi) \tag{4.1}$$

and describes the total amount of energy lost or gained in the RF system. Using a trigonometric identity this expression can be rewritten to

$$\Delta E_{\mathrm{RF}} = Ze\hat{U}_{\mathrm{eff}} \left[\sin(\phi_{\mathrm{RF,before}}) \cos(\Delta\phi) + \cos(\phi_{\mathrm{RF,before}}) \sin(\Delta\phi)\right]. \tag{4.2}$$

Assuming that both $\phi_{\mathrm{RF,before}}$ and $\Delta\phi$ are small angles, the cosine and sine can be approximated by $\cos(\phi_{\mathrm{RF,before}}) \approx 1$ and $\sin(\phi_{\mathrm{RF,before}}) \approx \phi_{\mathrm{RF,before}}$ and similarly for $\Delta\phi$ resulting in

$$\Delta E_{\mathrm{RF}} \approx Ze\hat{U}_{\mathrm{eff}} \left[\Delta\phi + \phi_{\mathrm{RF,before}}\right]. \tag{4.3}$$

Now there is the additional term with $\phi_{\mathrm{RF,before}}$ compared to equation 2.25 with the small

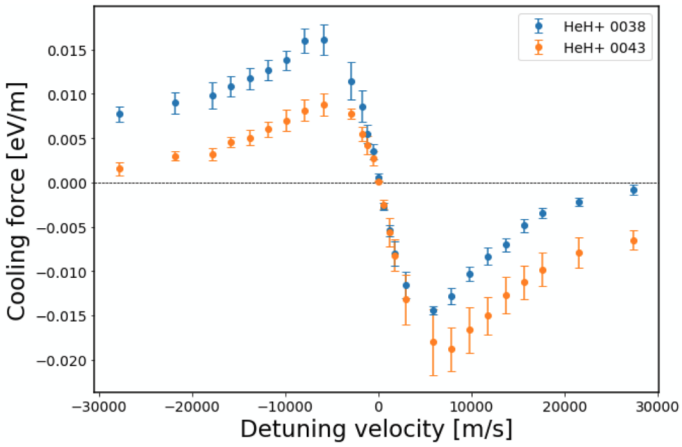

Figure 4.10: Effect of the bunching frequency on the cooling force. Comparison between run 0038 and 0043 of HeH^+, with bunching frequency changed from 412.526 kHz to 412.640 kHz.

angle approximation leading to the following equation for the cooling force

$$F_{\parallel} = -\frac{\Delta E_{\mathrm{RF}}}{l} = \frac{-Ze\hat{U}_{\mathrm{eff}}}{l}\left[\Delta\phi + \phi_{\mathrm{RF,before}}\right]. \tag{4.4}$$

In the measurement though only the phase shift $\Delta\phi$ was measured and used to create Figure 4.10, which describes the cooling force plus an additional term

$$\frac{-Ze\hat{U}_{\mathrm{eff}}}{l}\Delta\phi = F_{\parallel} + \frac{Ze\hat{U}_{\mathrm{eff}}}{l}\phi_{\mathrm{RF,before}} \tag{4.5}$$

and therefore the entire cooling force curve is expected to be shifted along the cooling force axis by this constant value.

The two resulting cooling force curves from the two HeH^+ runs are shown in Figure 4.10. The outcome is as expected: In run 0043 the cooling force curve is shifted downwards compared to run 0038 because of the additional term in equation 4.3. If one would shift the curve back up to compensate for this effect, the curve would not go through the origin. This is because in the calculation of the detuning velocity the fact that the velocities were not matched at first is not considered. They are calculated according to equation 2.27, in which E_{cool} is the energy of the electrons before the jump while it is assumed that the ion and electron velocities are matched. Since this is not the case when the RF frequency is changed, this equation would need to consider the offset energy E_{offset} of the electron beam compared to the ion beam at the start leading to

$$v_{\mathrm{det}} = \sqrt{2/m_{\mathrm{e}}}\left(\sqrt{E_{\mathrm{lab}}} - \sqrt{E_{\mathrm{cool}} + E_{\mathrm{offset}}}\right) \tag{4.6}$$

and thus the actual detuning velocities would be different from the ones used to create the cooling force curve. This means that the detuning velocity axis of the cooling force

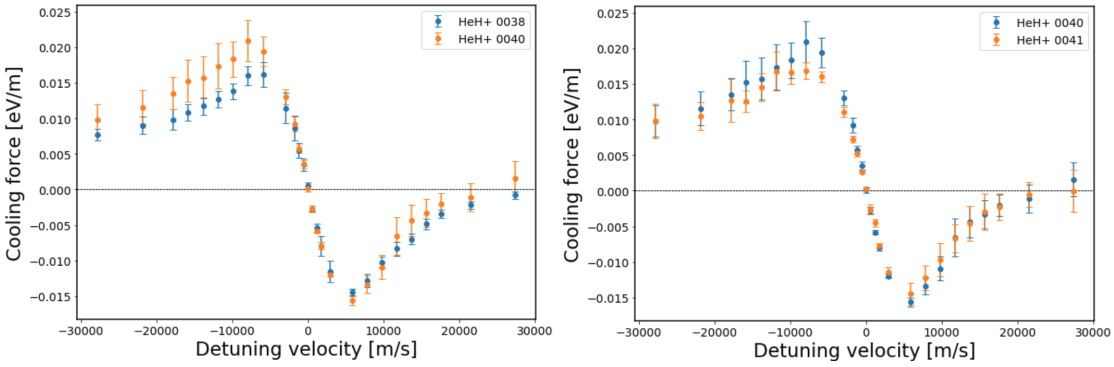

(a) (b)

Figure 4.11: Effect of ion current and electron beam position on the cooling force. Panel a): Comparison between run 0038 and 0040 of HeH^+, with stored ion number lowered by about 15 times. Panel b): Comparison between run 0040 and 0041 of HeH^+, with electron beam shifted horizontally changing overlap area with ion beam.

curve is expected to be shifted and distorted, which can be seen in Figure 4.10

The bunching frequency has also been adjusted between other HeH^+ runs ion order to match the ion revolution frequency. This is necessary, because the revolution frequency changes slightly but only between run 0038 and 0043 was the RF frequency changed intentionally to detune the velocities. Some of the other cooling force curves however are also shifted slightly which is most likely because this adjustment was not perfect.

Influence of the ion current

For the two HeH^+ runs, 0040 and 0041, the number of stored ions was lowered by about 15 times from $\sim 3.4 \cdot 10^7$ to $\sim 2.3 \cdot 10^6$. The effect of this is shown in Figure 4.11 a) where run 0038 and 0040 are compared. The change in ion current does not seem to have a big effect on the cooling force. The linear parts are very similar only towards higher detuning velocities they differ but not consistently.

But there is another effect of the number of ions in a bunch that becomes apparent when looking at the individual jumps. For every ion species, the phase after the jump has not stayed constant but changed continuously for example this can be seen in Figure 4.3 but also in Figure 4.12. This might be caused by a loss of ions after the jump. When the electron energy is changed during the jump, the ions are slowed down in the electron cooler and therefore reach the RF system later. If this delay is large, some ions might get pushed out of the stable phase space region called bucket, in which particles can be stored. Outside of the bucket the ions get lost. Now that the ion bunches consist of less particles, their longitudinal and transverse size would decrease, leading to a smaller and different overlap region with the electron beam. Since the average electron velocity increases towards the outside of the beam, due to their space charge potential, the ions would now be experienc-

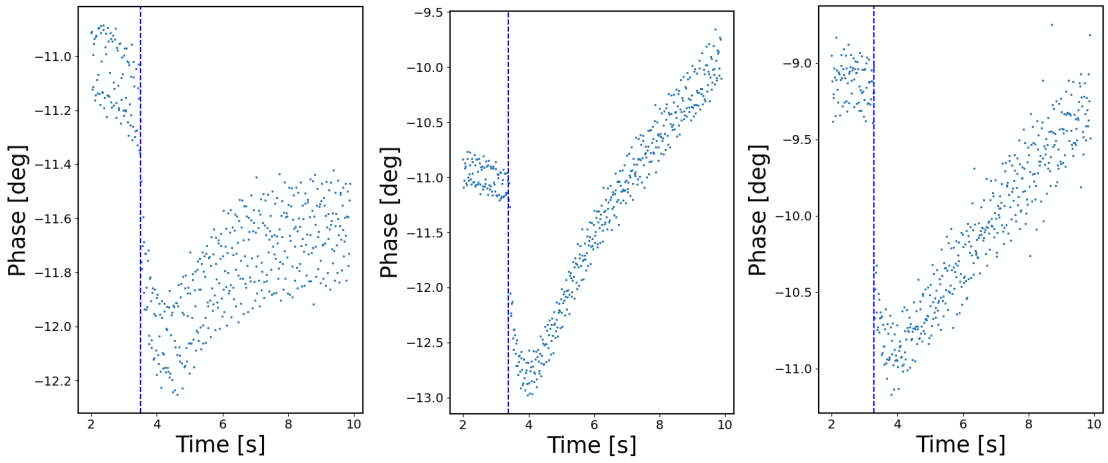

(a) (b) (c)

Figure 4.12: Effect of detuning velocity and ion current on phase development after jump. Panel a): run 0038 with a detuning velocity of $\sim -1200\,\frac{\mathrm{m}}{\mathrm{s}}$. Panel b): run 0038 with a detuning velocity of $\sim -2900\,\frac{\mathrm{m}}{\mathrm{s}}$. Panel c): run 0040 with same detuning velocity as in panel b) but lower ion current.

ing a different cooling force, causing a change in ion velocity and with it a change in phase.

Firstly this would mean, that this continuous phase change after the jump due to a loss of ions depends on the cooling force and therefore on the detuning velocities and secondly, that a reduced number of ions to begin with would also decrease this effect. Both of these predictions can be seen in 4.12: For a smaller absolute value of the detuning velocity of $\sim -1200\,\frac{\mathrm{m}}{\mathrm{s}}$ in a) the continuous phase change after the jump is reduced compared to the larger absolute value of the detuning velocity of $-2900\,\frac{\mathrm{m}}{\mathrm{s}}$ in b). Here the cooling force is larger and thus the ions are slowed more and more ions are lost. With less ions at the start and the same detuning velocity as in b), the phase rises slower than in b). This is shown in c).

This behavior should change for detuning velocities past the points of maximal absolute cooling force. Past these points the energy loss in the cooler reduces again, which should lead to a slower steady increase in phase after the jump. This however can not be seen in these graphs, where the phase after the jump still rises fast. With a small detuning velocity and a lower ion current the phase stays mostly constant even after the jump.

Influence of the electron beam position

Now the influence of the electron beam position is described. This was done in order to examine the effect of dispersive cooling, which is explained in detail by Beutelspacher *et al.* 2003.

Dispersive cooling uses the dispersion of the ion beam, meaning the horizontal beam

position depends on the ion beam momentum. Thus a change in longitudinal momentum $\Delta p_{\parallel}$ of an ion leads to horizontal displacement Δx of the ion given by

$$\Delta x = D_S \frac{\Delta p_{\parallel}}{p_{\parallel}} \tag{4.7}$$

where $p_{\parallel}$ is the longitudinal ion momentum in the laboratory frame and D_S is the dispersion.

The electron beam produced by the electron cooler has parabolic velocity profile due to its space charge potential, meaning the electron velocity and thus the cooling force depends on the transverse position within the beam. Usually the ion beam is in the center of the electron beam where the velocity gradient is negligible. Changing the horizontal electron beam position compared to the ion beam creates a horizontal gradient of the longitudinal cooling force, because now the ion beam sees one flank of the electron velocity distribution.

The combination of the ion beam dispersion and the horizontal gradient of the longitudinal cooling force can be used to dampen the horizontal betatron oscillations. A positive momentum transfer to an ion while it is more ring outwards leads to a reduction of the betatron oscillation as well as a negative momentum transfer while it is ring inwards. Using the gradient of the longitudinal cooling force it can be achieved, that ions interact with faster electrons while towards the outside of the ring and therefore receiving a positive momentum change and that they interact with slower electrons while ring inwards and thus receiving a negative momentum change. This means that displacing the electron beam ring inwards compared to the aligned state is expected to decrease the longitudinal cooling force but increase the horizontal cooling force. Shifting the beam outwards, achieves the opposite.

In this experiment the horizontal electron beam position was shifted about 0.325 mm outwards using the horizontal steering coils mentioned in section 3.1 between the runs HeH^+ runs 0040 and 0041. The two resulting cooling force curves are shown in Figure 4.11 b). Here it was expected to see a larger longitudinal cooling force in run 0041 compared to run 0040, which was not the case. This could be because the electron beam was not shifted enough to reach a sufficient gradient of the longitudinal cooling force. This test could be repeated in the future with multiple different position shifts of the electron beam to get a more complete picture of dispersive cooling.

Influence of the precooling time

Afterwards the two HeH^+ runs 0041 and 0042 are compared to analyse the effect that the cooling time before the jump has on the cooling force. In theory this should not change the cooling force and was done only as a check, whether the ion beam was fully cooled before the jump happened or not. If this is not the case the ion bunches see a larger part of the electron beam with different velocities causing a change in cooling force. The result is shown in Figure 4.13, where no significant difference in cooling force is visible. In this particular case, a cooling time of 3 s seems to be long enough.

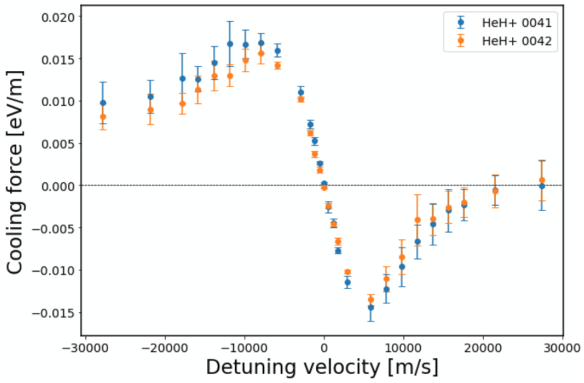

Figure 4.13: Effect of the precooling time on the cooling force. Comparison between HeH^+ runs 0041 and 0042 with cooling time increased from 3 s to 6 s.

Influence of the magnetic field in the interaction zone

Lastly, the effect of the magnetic field strength in the interaction zone is analysed. Not only the magnetic field in the interaction zone is increased, but also in the rest of the electron cooler, thus not affecting the expansion factor α or the electron beam radius, which would directly affect the cooling force.

This was done, because in a previous experiment it was suspected that electron temperature changes with the magnetic field strength. The electron temperature affects the peak position and also slightly the amplitude of the cooling force curve, which can be determined with a cooling force measurement and thus this suspicion could be confirmed or ruled out.

A strong magnetic field is necessary in an electron cooler to guide the electron beam and suppress unwanted effects (see Shornikov 2012). It also allows for an adiabatic transport of the electron beam, which is necessary because it stops non-adiabatic heating effects. If the field was too small the transverse electron temperature would increase as a consequence.

To test this the magnetic field was doubled between the Ne^{2+} runs 0199 and 0205 from from 0.005 to 0.01 T, with the results shown in Figure 4.14. For Ne^{2+} two methods were used for determining the jump size, either using the point after a certain time after the jump or the point at the first peak shortly after the jump. In the case of run 0205 the first method did not result in a good cooling force curve as shown in Figure 4.14 b) due to very undefined phase jumps, the first peak method however was more reliable and was therefore used for the analysis also for run 0199 and is shown in Figure 4.14 a).

Since it is uncertain whether this first peak has any physical significance or not, it is difficult to rely on these results. However, a qualitative comparison between the two curves might be justified, where a shift of the extrema can be found. In run 0205 the cooling force peaks are closer to zero, which could infer a lower electron temperature than in run 0199.

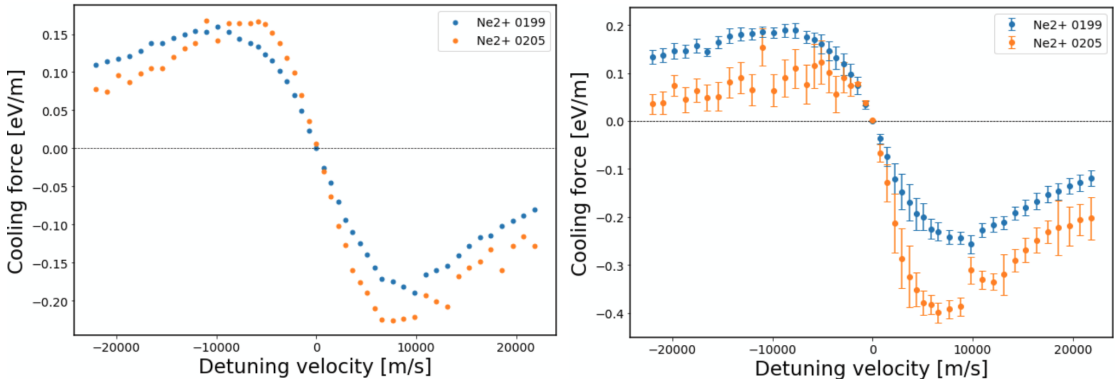

(a) (b)

Figure 4.14: Effect of the magnetic field on the cooling force. Comparison between Ne^{2+} runs 0199 and 0205 with magnetic field increased in the latter. Panel a): cooling curves created using the first peak seen in Figure 4.7. Panel b): cooling curve using the fit method.

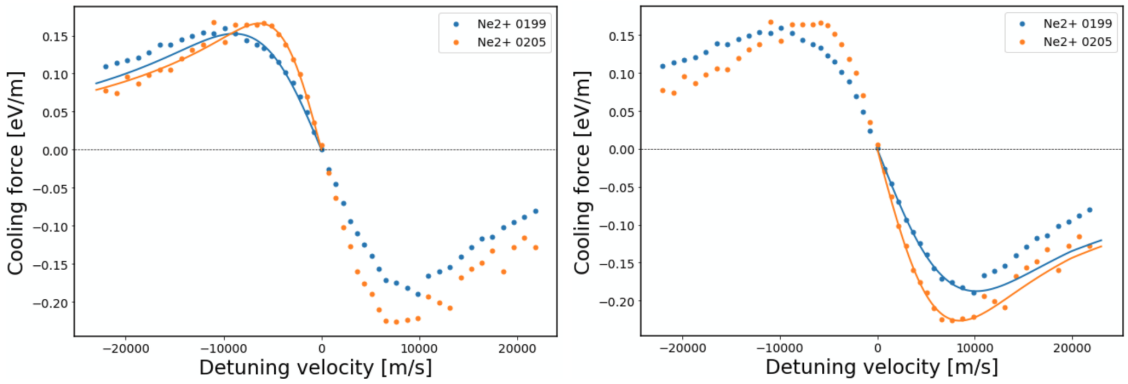

(a) (b)

Figure 4.15: Cooling curves from the Ne^{2+} runs 0199 and 0205 with theoretical curves overlapped. The blue curve was fitted to the blue data points of run 0199 and the orange curve to run 0205. Since the curves are not symmetrical, panel a) shows the fits to the maxima for negative velocities and panel b) shows the fit to the minima for positive velocities. Results of the fits are given in the main text.

To try and quantify this effect the theoretical model from section 2.2 was used to create simulated cooling force curves by numerically integrating equations 2.17 and 2.18. These curves were fitted to both cooling force curves as described in section 4.4 by varying the longitudinal electron temperature and scale. This was done separately for the maximum and the minimum by only considering points for the fit that are between the origin and the maximum or minimum. The longitudinal electron temperature is the parameter that affects the peak position and the scale only affects the amplitude, which is not considered here. The other parameters that were used for the fits can be found in table 4.3. The value for the longitudinal electron temperature given in this table is the calculated value and was varied by the fitting algorithm. For fits of the maxima shown in Figure 4.15 a) the resulting longitudinal temperatures were $k_B T_{e,\parallel} = 149\,\mu\text{eV}$ for run 0199 and $k_B T_{e,\parallel} = 64\,\mu\text{eV}$ for run 0205. The fits using the minima are shown in 4.15 b) with the temperatures $k_B T_{e,\parallel} = 205\,\mu\text{eV}$ for run 0199 and $k_B T_{e,\parallel} = 131\,\mu\text{eV}$ for run 0205.

There seems to be a reduction of the longitudinal electron temperature of at least $\sim 40\,\%$ caused by the increase in magnetic field. This however is based on the non-magnetic model from section 2.2 that does not include the magnetic field. So this difference in peak position might be caused by effects that are not considered in this model.

Influence of the direction of the jump

Another property that all of these cooling force curves have in common is their asymmetry. For positive detuning velocities the absolute value of the cooling force tends to be lower than for negative detuning velocities. Also the shape of the peak is different. The minimum is usually sharper than the maximum, which sometimes looks like the top has been cut off. This is especially apparent for the ArH^+ cooling curve in Figure 4.4 b). The question is whether the asymmetry depends on the detuning velocity or the sign of the phase jump $\Delta\phi$. To test this, the first and second jump of the Xe^{3+} data set can be compared.

During the Xe^{3+} measurements the electron energy was changed to the set value and 15 s later back to original value as shown in Figure 4.1 a). The same detuning velocity should be attributed to the jump going back to the starting energy value, as to the first jump to the detuned energy value. What changes between two jumps are the values for $\phi_{\text{RF,before}}$ and $\phi_{\text{RF,after}}$ as described in section 4.3. Usually equation 2.25 is used, assuming $\phi_{\text{RF,before}} = 0$ and $\phi_{\text{RF,after}} = \Delta\phi$, but for the jump back these two are switched: $\phi_{\text{RF,before}} = \Delta\phi$ and $\phi_{\text{RF,after}} = 0$. Thus equation 2.25 needs to be changed to

$$\begin{aligned} \Delta E_{\text{RF}} = \Delta E_{\text{RF,after}} - \Delta E_{\text{RF,before}} &= Ze\hat{U}_{\text{eff}} \sin(\phi_{\text{RF,after}}) - Ze\hat{U}_{\text{eff}} \sin(\phi_{\text{RF,before}}) \\ &= 0 - Ze\hat{U}_{\text{eff}} \sin(\Delta\phi) \end{aligned} \tag{4.8}$$

which changes the sign of the energy gained in the RF system ΔE_{RF} and therefore of the cooling force compared to equation 2.25 and 2.26 to

$$F_{\parallel} = -\frac{\Delta E_{\text{RF}}}{l} = Ze\hat{U}_{\text{eff}} \sin(\Delta\phi)/l \tag{4.9}$$

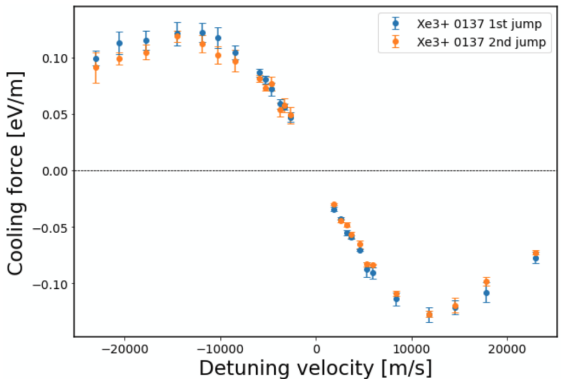

Figure 4.16: Cooling force curve of the Xe^{3+} run 0137 using the second jump as shown in Figure 4.1 d) as well as the first jump.

For energy jumps from a detuned energy to the cooling energy the equation above needs to be used, which differs only in the sign compared to equation 2.26.

This second jump was also used to create a cooling force curve for the Xe^{3+} run 0137 with the equation above, which is shown in Figure 4.16 as well as the corresponding cooling force curve of the first jump. The difference between the two curves is that for the same detuning velocity the phase jumps $\Delta\phi$ have the opposite sign. Thus if the shape matches it does not depend on the direction of the phase jump but rather on the detuning velocity. The two curves are very similar with the curve belonging to the second jump having a slightly lower amplitude. This is most likely due to the fact, that after the first jump the phase variance increases as seen in Figure 4.1 a), leading to a less defined second jump. Also in contrast to what one would expect, the phase after the second jump is not equal to the phase before the first jump.

The shape of the cooling force curves created from the second jump matches the shape of the curve from the first jump as seen in Figure 4.16. This proves that the phase jump size is independent of the sign as long as one jumps to or from the same electron velocity. On the other hand, jumping in a different direction with the electron velocity initially, changes the result, leading to the previously mentioned asymmetry in the cooling force curves. The origin of that asymmetric behavior is not yet understood and motivates further measurements.

4.4. Comparison with a theoretical model

In this section the cooling curves of the various ions are compared with simulated ones created by numerically integrating equations 2.17 and 2.18 from section 2.2. The necessary parameters used for each data set are listed in table 4.3. The electron density and temperatures were calculated based on other electron cooler settings such as electron current or interaction zone potential.

To compare the simulated with the experimental cooling force curves they are plotted on top of each other using the parameters from table 4.3. Additionally, two simulated curves are fitted to the data by varying the scaling factor ψ and the longitudinal electron temperature $k_B T_{e\parallel}$ using the least squares method. One fit considers only points between the origin and the maximum while the other one does the same for the minimum. The peak position depends on the longitudinal electron temperature, the electron density and the ion charge. The influence of the last two parameters however is negligible compared to the effect of the electron temperature. This is how by determining the peak position the calculated longitudinal electron temperature can be compared with the one according to the model.

In Figure 4.17 a) the result for the Xe^{3+} run 0136 is shown. The fit of the maximum yielded a longitudinal electron temperature of $k_B T_{e\parallel,\max} = 270\,\mu\text{eV}$ and a scaling factor $\psi_{\max} = 1.2$ compared to the fit of the minimum with $k_B T_{e\parallel,\min} = 304\,\mu\text{eV}$ and $\psi_{\max} = 1.5$. Both of the temperature values are larger than the expected value of $k_B T_{e\parallel,\text{calc}} = 242\,\mu\text{eV}$.

Secondly, this was done for the ArH^+ run 0038 shown in Figure 4.17 b). Here, the resulting fit parameters were $k_B T_{e\parallel,\max} = 129\,\mu\text{eV}$ and $\psi_{\max} = 1.4$ for the maximum along with $k_B T_{e\parallel,\min} = 329\,\mu\text{eV}$ and $\psi_{\max} = 2.9$ for the minimum. The cooling force curve is very asymmetric, which is reflected by the fit parameters. The value of $k_B T_{e\parallel,\min}$ is more than twice as big as the one of $k_B T_{e\parallel,\max}$. The same is true for the scaling factors $\psi_{\min}$ and $\psi_{\max}$. The calculated value lies between the two and is $k_B T_{e\parallel,\text{calc}} = 256\,\mu\text{eV}$. Also visually the fit of the minimum is much worse and data points past the minimum are not covered at all by the fit, like it is the case for Xe^{3+}. This can probably be explained by the fact, that ArH^+ was the first ion used for cooling force measurements within the course of this thesis and thus the measurement was less optimized. Therefore, additional measurements with ArH^+ could determine whether this result was due to a lack of experience.

The result of the HeH^+ run 0038 is shown in Figure 4.18 a). The fit parameters came out to be $k_B T_{e\parallel,\max} = 52\,\mu\text{eV}$ and $\psi_{\max} = 1.7$ for the maximum as well as $k_B T_{e\parallel,\min} = 51\,\mu\text{eV}$

Ion	Ion mass[u]	Ion charge	Electron density[$\frac{10^5}{\text{cm}^3}$]	$k_B T_{e\parallel}$[μeV]	$k_B T_{e\perp}$[meV]
Xe^{3+}	128.90	3	4.167	242.18	2.25
ArH^+	40.97	1	4.193	256.75	2.25
HeH^+	5.01	1	1.508	94.48	2.25
Ne^{2+}	19.99	2	8.671	113.01	2.25

Table 4.3: Parameters of the different ions used in the theoretical model.

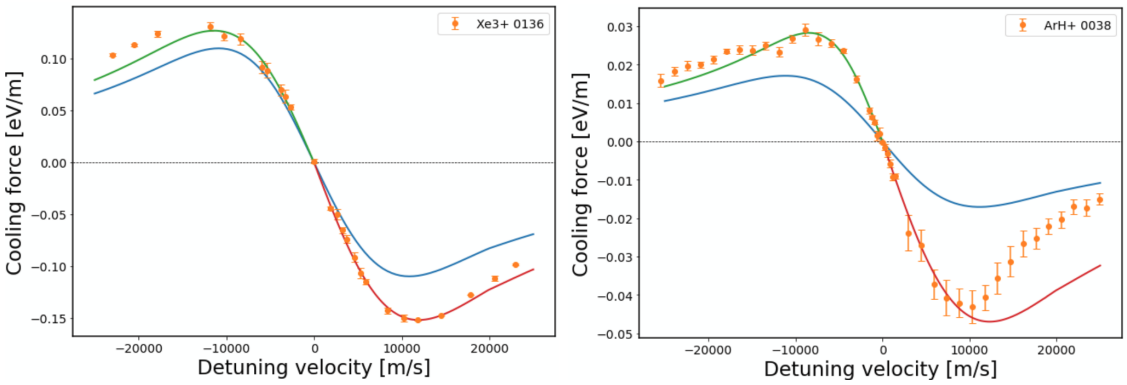

(a) (b)

Figure 4.17: Simulated and experimental cooling force curves for Xe^{3+} and ArH^{+}. Blue curve uses the parameters from table 4.3. The green and red curves are fitted to the positive and negative branch, respectively, limiting the fitting range between the origin and the peak extreme. The parameters gained from the fits are in table 4.4. Panel a): Xe^{3+} curve from run 0136. Panel b): ArH^{+} curve from run 0038.

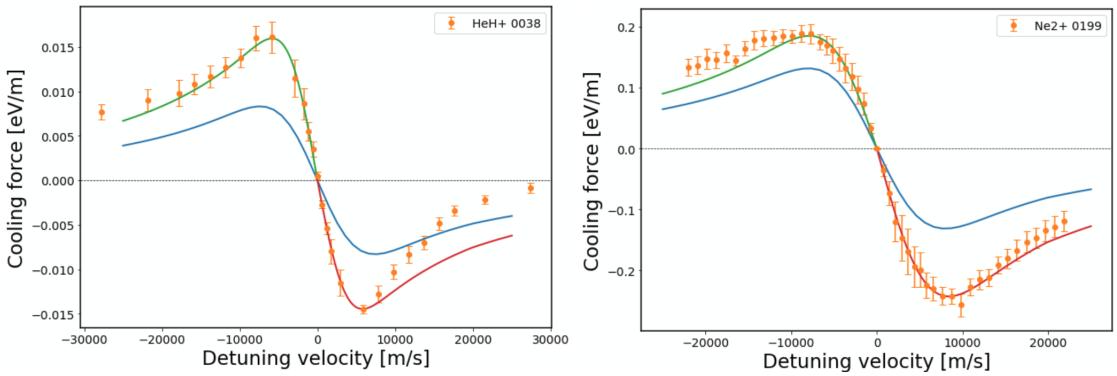

(a) (b)

Figure 4.18: Simulated and experimental cooling force curves for HeH^{+} and Ne^{2+}. Blue curve uses the parameters from table 4.3. The green and red curves are fitted to the positive and negative branch, respectively, limiting the fitting range between the origin and the peak extreme. The parameters gained from the fits are in table 4.4. Panel a): HeH^{+} curve from run 0038. Panel b): Ne^{2+} curve from run 0199.

Data set	Calculated $k_B T_{e\parallel,\mathrm{calc}}[\mu\mathrm{eV}]$	Fit of maximum $k_B T_{e\parallel,\mathrm{max}}[\mu\mathrm{eV}]$	Fit of minimum $k_B T_{e\parallel,\mathrm{min}}[\mu\mathrm{eV}]$	ψ_{max}	ψ_{min}
Xe^{3+} run 0136	242	270	304	1.2	1.5
ArH^+ run 0038	256	129	329	1.4	2.9
HeH^+ run 0038	94	52	51	1.7	1.6
Ne^{2+} run 0199	113	109	129	1.4	1.9

Table 4.4: Resulting electron temperature and scaling factors of fitting the maxima and minima with the theoretical model.

and $\psi_{\mathrm{max}} = 1.6$ for the minimum. Already one can see that this result is much better than the one of ArH^+. The parameters for the minimum and maximum are almost identical, but still different from the calculated value $k_B T_{e\parallel,\mathrm{calc}} = 94\,\mu\mathrm{eV}$, and also visually the fit looks more accurate. Especially the data points of maximum are described well even past the maximum despite them not being included in the fitting algorithm. Only the minimum shows the same behaviour where the cooling force decreases faster than predicted.

Lastly the Ne^{2+} run 0199 was fitted, which is shown in Figure 4.18 b). Here the values $k_B T_{e\parallel,\mathrm{max}} = 109\,\mu\mathrm{eV}$ and $\psi_{\mathrm{max}} = 1.4$ were output by the fit of the maximum and $k_B T_{e\parallel,\mathrm{min}} = 129\,\mu\mathrm{eV}$ and $\psi_{\mathrm{max}} = 1.9$ by the fit of the minimum. Both of these temperatures are similar to the expected value of $k_B T_{e\parallel,\mathrm{calc}} = 113\,\mu\mathrm{eV}$.

In general it is interesting to observe similarities between the fits of the singly charged ions ArH^+ and HeH^+ and the multiply charged ions Xe^{3+} and Ne^{2+}. For the former the fit does not describe the shape of the minimum as well as for the latter ions. They all have in common that the peak of the maximum is not as large as the peak of the minimum. This is shown by the fact, that the scaling factor ψ_{max} from the fit of the maximum is smaller than ψ_{min} from the fit of the minimum. Only for HeH^+ ψ_{max} is slightly larger than ψ_{min}. For all simulated curves ψ is larger than 1.0, which is to be expected, since the model does not include the effect of the magnetic field in the interaction region, that would increase the predicted cooling force. This is also expected to change the shape of the curve, which could be an explanation for the poor fit of the data past the minima of the ArH^+ and HeH^+ examples.

Using the fits the longitudinal electron temperature could be determined. These values for the different data sets are summarized in table 4.4 and can be compared to the calculated values. Here deviations of up to 50 % in the case of ArH^+ were found, only for Ne^{2+} the temperatures from the fits did not differ much from the expected values. This could indicate a flaw in the analytical calculation of the electron temperature. Another possibility is that the model does not predict the peak position correctly and for a different model the peaks would match using the calculated electron temperatures. Nevertheless, all observed temperatures are on the same order as the predicted ones.

Next the peak-to-peak value of the experimental curves will be compared to peak-to-peak value of the equivalent simulated curve by dividing the former by the latter resulting in the ration α. As parameters for the theoretical curves the calculated values listed in

Data set	α_{calc} using $k_B T_{e\parallel,\text{calc}}$	α_{max} using $k_B T_{e\parallel,\text{max}}$	α_{min} using $k_B T_{e\parallel,\text{min}}$
Xe^{3+} run 0136	1.29 ± 0.02	1.33 ± 0.02	1.37 ± 0.02
ArH^{+} run 0038	2.11 ± 0.13	1.79 ± 0.11	2.26 ± 0.14
HeH^{+} run 0038	1.84 ± 0.11	1.66 ± 0.10	1.65 ± 0.10
Ne^{2+} run 0199	1.69 ± 0.09	1.68 ± 0.09	1.74 ± 0.09

Table 4.5: Peak-to-peak ratios α between experimental and simulated curves.

table 4.3 will be used. This will be repeated twice by using the longitudinal electron temperatures gained from the fits found in table 4.4. The resulting ratios are given in table 4.5. The errors, that are given, are derived from the error bars of the experimental curves. These errors are used to calculated the errors of the peak-to-peak value, which are propagated to the peak-to-peak ratio using the gaussian error propagation.

The resulting values of α are similar to the scaling factors ψ in table 4.4, which is to be expected. The advantage of these ratios over the scaling factors is that they are not influenced by the asymmetry of the curves. If the curve was shifted up or down due to imperfect matching of the bunching frequency, ψ_{max} and ψ_{min} would be different, unlike α, which would be unaffected. Ideally the values for α are the same for each ion species, in that case it would be possible to predict the experimental amplitude of the cooling force by simply scaling up the simulated curve. Here however, not all ratios are the same, although they are all between 1.2 and 2.3. This means it is at least possible to predict, that the peak-to-peak value will be larger than the simulated one by usually not more than a factor of 2.

Lastly the dependence of the cooling force amplitude on various parameters is examined. According to equation 2.17 the cooling force amplitude depends on the charge state Z through the factor Z^2 but also through the Coulomb logarithm. The same is true for the dependence on the electron density n_e. To check whether scaling the curve simply by $Z^2 n_e$ is a sufficient approximation, a normalized cooling force is introduced. This will identify the impact of Z and n_e through the Coulomb logarithm and determine if it is negligible. The normalized cooling force is calculated by dividing the cooling force according to equation 2.17 by Z^2 and n_e:

$$\begin{aligned} F_{\parallel,\text{norm}}(v_r') &= \frac{F_\parallel(v_r')}{Z^2 n_e} \\ &= -\frac{e^4}{4\pi\epsilon_0^2 m_\text{e}} \int_0^{2\pi} \int_{-5\Delta_{e\parallel}}^{5\Delta_{e\parallel}} \int_0^{5\Delta_{e\perp}} L_C f(\vec{v}_e) \frac{v_r' - v_{e\parallel}}{\sqrt{\left(v_r' - v_{e\parallel}\right)^2 + v_{e\perp}^2}^3} v_{e\perp} \cdot d\phi dv_{e\parallel} dv_{e\perp} \end{aligned} \tag{4.10}$$

Now this equation is used to create a simulated cooling force curve for each ion type based using the parameters from table 4.3. Any differences in amplitude in those curves is therefore caused by the effect of the Coulomb logarithm or the longitudinal electron tem-

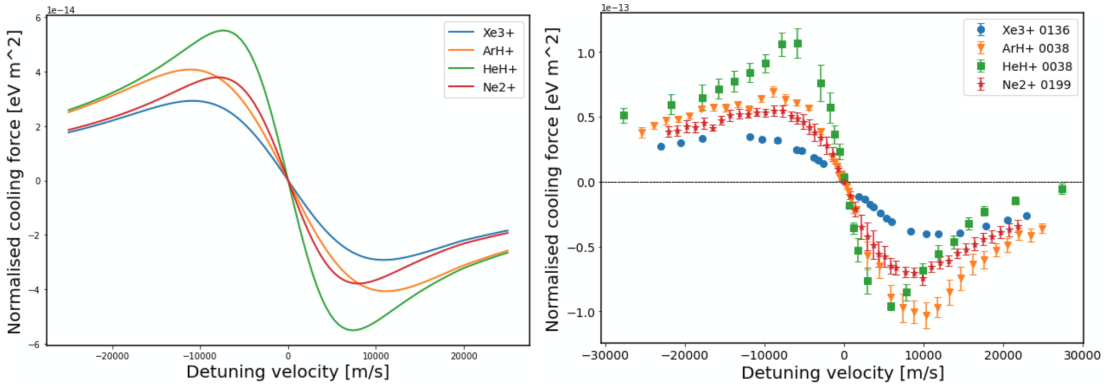

(a) (b)

Figure 4.19: Panel a): Normalized simulated cooling force curves $F_{\parallel,\mathrm{norm}}(v_r')$ of the different ion types. Panel b): Normalized experimental cooling force curves of the different ions.

perature, which also has an effect on the amplitude. The resulting simulated normalized cooling force curves are shown in Figure 4.19 a). The resulting amplitudes vary in size by up to a factor of 2. Interesting to observe is, that the amplitudes of the simulated curves for ArH^+ and Xe^{3+} have a significantly different size. This is only due to the dependence on Z within the Coulomb logarithm, since the electron density n_e and temperatures $k_B T_{e\parallel}$ are very similar and only the ion charge Z is different between these two ion.

In general the scaling of the cooling force amplitude with n_e and Z is not just caused by the simple factor $Z^2 n_e$ but also the Coulomb logarithm has a significant impact. The relative amplitudes of the simulated normalized curves can also be compared to the equivalent experimental curves. They are shown in Figure 4.19 b). The relative size of the experimental amplitudes are very similar to the predicted ones. Xe^{3+} has the smallest amplitude in both parts of Figure 4.19, followed by Ne^{2+}. The curves of HeH^+ are also the largest in both cases, only the experimentally determined minimum of ArH^+ does not agree with the simulated one. In general this binary collision model describes the relative amplitudes between different ion species rather well.

5. Conclusion and Outlook

In the storage ring CSR the electron cooler provides an electron beam that is overlapped with the ion beam over a defined distance. This can apply electron cooling to the beam, which improves the ion beam quality by reducing its longitudinal and transverse energy spread as well as the transverse size. Thus a quick and easy measurement procedure is necessary for optimising the cooling force. This is why the goal of this bachelor thesis was to implement and test a cooling force measurement method, called the phase shift method, by analysing data acquired using this technique. During this task, a software program was developed to automate the data recording and analysis process, allowing for uncomplicated cooling force measurements.

Multiple measurements of the same ion species but with different settings of the electron cooler and other systems were performed in order to evaluate the reliability of the cooling force measurement method. The results were presented in section 4. They were analysed for systematic effects caused by various settings and compared with simulations based on a theoretical model.

Most of the results compare well to the model of the cooling force, though not all behaviour was understood in all detail. E.g. it was expected that the effective bunching voltage does not change the cooling force. However, doubling the effective bunching voltage lead to an increase in cooling force amplitude by about 30 % for HeH^+ but in the case of Xe^{3+} the amplitude decreased by about 15 % after an increase of the bunching voltage by about 80 %. It was also found, that doubling the magnetic field in the electron cooler changes the peak position of the curves, which could indicate a change in longitudinal electron temperature.

Overall it was shown that this measurement method works and can be used to record cooling force curves, even at very low cooling energies down to $\sim 4\,\mathrm{eV}$. Since the addition of the software, a measurement of the full cooling force curve takes between 20 and 30 minutes depending on the number of points. For optimization purposes only a couple of points need to be covered, reducing the necessary time to only a few minutes. Along with a simple data analysis tool, allowing for quick feedback after the measurement, it is possible to adapt to the results between measurements. This way systematic measurements like cooling force optimizations are easy to accomplish.

Even though the influence of some parameters on the amplitude, like the effective bunching voltage, can not be explained yet, this measuring technique is still expected to be usable for electron cooling optimization by comparing the relative cooling force curves while changing various settings. Throughout the process of measuring the cooling force, the quality of data improved, due to a better understanding of the optimal conditions. For example, a stable ion beam is important for obtaining reliable data and thus smaller phase jumps are preferred as it was the case for Xe^{3+}.

In the future, more systematic studies on this cooling force measurement method under various, even more extreme conditions are planned, where the observations indicated in

this thesis will be a valuable baseline.

A. Recording software

In the course of this bachelor thesis a recording software was developed, that automates the recording of data of the SR860 500 kHz DSP Lock-in Amplifier. It uses the "data capture" feature of the Lock-in amplifier, which allows it to record a specified amount of data with a certain sample rate that can be translated into a capture duration. The most important Lock-in settings can be set using the interface. It can start the recording either immediately after the button is pressed or wait for an external trigger to the lock-in to start recording. After one set of data has been recorded it is transferred to a computer where it is stored as a csv file. The amount of times this process is repeated can also be set. The trigger method was used to coordinate the start of recording with the electron energy jump. Based on the capture rate the time after the start of recording can be calculated for each point which is also included in the file.

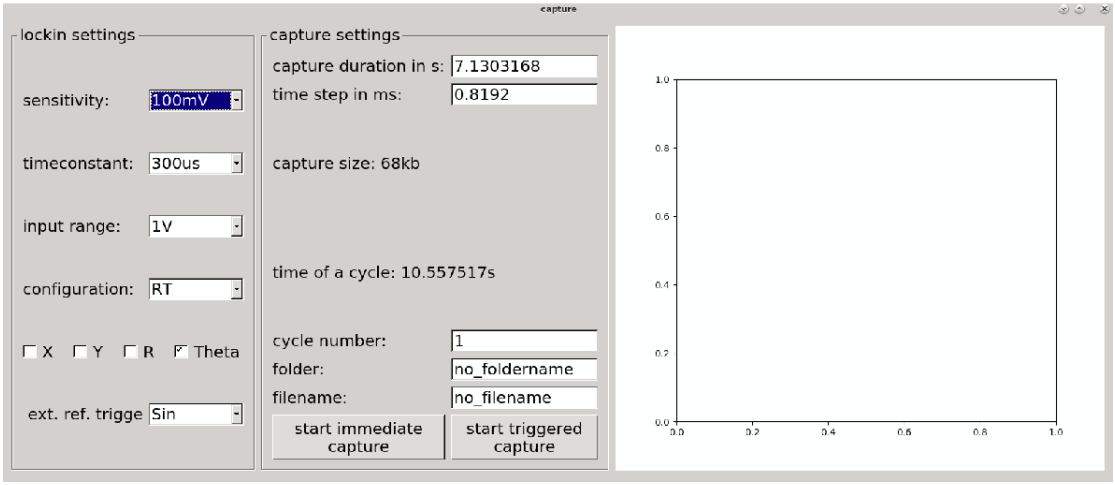

Figure A.1: Capture software

References

1. Becker, A. *Imaging of Neutral Fragmentation Products from Fast Molecular Ion Beams: Paving the Way for Reaction Studies in Cryogenic Environment* PhD thesis (Jan. 2016).
2. Beutelspacher, M., Grieser, M., Noda, K., Schwalm, D. & Wolf, A. Dispersive electron cooling experiments at the heavy ion storage ring TSR. *Nuclear Instruments and Methods in Physics Research Section A: Accelerators, Spectrometers, Detectors and Associated Equipment* **512,** 459–469 (Oct. 2003).
3. Beutelspacher, M. *Systematische Untersuchungen zur Elektronenkuehlung am Heidelberger Schwerionenspeicherring TSR* in (2000).
4. Budker, G. I. An effective method of damping particle oscillations in proton and antiproton storage rings. *Soviet Atomic Energy* **22,** 438–440 (1967).
5. Danared, H. Electron cooling at CRYRING with an expanded electron beam. *Nuclear Instruments & Methods in Physics Research Section A-accelerators Spectrometers Detectors and Associated Equipment* **391,** 24–31 (1997).
6. Derbenev, Y. S. & Skrinsky, A. N. THE EFFECT OF AN ACCOMPANYING MAGNETIC FIELD ON ELECTRON COOLING. *Particle Accelerators* **8,** 235–243 (1978).
7. Paul, D. *Electron recombination studies of rotationally cold CH+ ions at the Cryogenic Storage Ring* PhD thesis (Jan. 2021).
8. Poth, H. Electron cooling: Theory, experiment, application. *Physics Reports* **196,** 135–297. ISSN: 0370-1573. https://www.sciencedirect.com/science/article/pii/0370157390900409 (1990).
9. Shornikov, A. An electron cooler for ultra-low energy cryogenic operation (Jan. 2012).
10. Snow, T. & McCall, B. Diffuse Atomic and Molecular Clouds. *Annual Review of Astronomy and Astrophysics* **44,** 367–414 (Aug. 2006).
11. Spruck, K. *et al.* An Efficient, Movable Single-Particle Detector for Use in Cryogenic Ultra-High Vacuum Environments. *The Review of scientific instruments* **86** (Nov. 2014).
12. Vogel, S. *Developments at an Electrostatic Cryogenic Storage Ring for Electron-Cooled keV Energy Ion Beams* PhD thesis (Jan. 2016).
13. Von Hahn, R. *et al.* The cryogenic storage ring CSR. *Review of Scientific Instruments* **87,** 063115. ISSN: 1089-7623. http://dx.doi.org/10.1063/1.4953888 (June 2016).
14. Wilhelm, P. *First Studies of Low-Energy Electron Cooling of keV Energy Ion Beams at the Electrostatic Cryogenic Storage Ring CSR* PhD thesis (Jan. 2019).

Erklärung

Hiermit versichere ich, dass ich die vorliegende Arbeit selbstständig verfasst und keine anderen als die angegebenen Quellen und Hilfsmittel benutzt habe, dass alle Stellen der Arbeit, die wörtlich oder sinngemäß aus anderen Quellen übernommen wurden, als solche kenntlich gemacht und dass die Arbeit in gleicher oder ähnlicher Form noch keiner Prüfungsbehörde vorgelegt wurde.

Heidelberg, den 3 April 2022 ..... Jonas Bechtel .....